# Automatic Determination of Cuttings and Cavings Properties for Hole Cleaning and Wellbore Stability Assessment Using a Laser-Based Sensor

**Abraham C. Montes[1]*, Santiago Callerio[1], Çınar Turhan[1], Asad Safarov[1], Pradeepkumar Ashok[1], and Eric van Oort[1]**

[1]Hildebrand Department of Petroleum and Geosystems Engineering, The University of Texas at Austin

## Summary

This work describes an accurate method for the automatic, real-time characterization of cuttings and cavings, including their volume, size distribution, and shape/morphology. This method integrates high-resolution images and 3D data (points in 3D space), collected in real time using an integrated laser-based sensor previously tested in the field. In addition, we analyze the effect of the morphological characteristics of cuttings/cavings on the estimated void space between them when they are stacked.

The proposed method encompasses (1) the identification of individual cuttings/cavings in the data (segmentation), (2) the extraction of their morphological characteristics, and (3) the estimation of their bulk volume, as well as their effective volume (without the interstitial void space) when these are stacked. To achieve these outputs, our method incorporates (1) optimized image preprocessing methods, (2) state-of-the-art computer vision techniques, (3) ellipse-fitting algorithms, and (4) numerical integration of the 3D data. We validated the proposed method at laboratory scale, simulating challenging field conditions that included poor mud/solids separation and stacked cuttings.

The assessment of the hole cleaning sufficiency and wellbore stability is key to preventing undesirable nonproductive time (NPT) events in drilling operations, such as stuck pipe events. The conventional method for such an assessment involves low-frequency sampling of cuttings/cavings from collector trays at the rig shale shakers, as well as their manual characterization by a human. This person infers volume, size distribution, and morphological characteristics of the returning solids stream. This approach results in a biased and often late evaluation of hole cleaning and wellbore stability issues, thereby missing out on opportunities to prevent NPT. Our method enables an accurate real-time characterization of cuttings/cavings, even in challenging conditions such as wet and stacked solids. Additionally, we observed that, when the cuttings/cavings are stacked, the required correction to the initial volume estimation (derived from the integration of the 3D data) depends on their morphological characteristics, as well as the level of stacking. Because our proposed method covers these aspects, it can also provide an accurate measurement of the solids' volume, serving as the basis for a timely and accurate evaluation of hole cleaning sufficiency and wellbore stability.

This work is the first to propose a holistic, automatic, and real-time characterization of cuttings/cavings, including their volume, size distribution, and shape/morphology. Furthermore, it is the first to integrate 3D data with high-resolution images to pursue this objective. The method proposed in this paper can be used for the real-time assessment of hole cleaning sufficiency and wellbore stability, and, consequently, for the prediction, prevention, and better management of NPT-producing events.

## Introduction

The characterization of returning solids in drilling operations is crucial for assessing the wellbore condition and diagnosing potential problems, such as wellbore instability and insufficient hole cleaning. Traditionally, this characterization is performed manually by a human who analyzes samples collected at a low frequency from the shale shakers. This approach has two notable shortcomings. First, it may introduce bias in the evaluation of cuttings and cavings due to subjectivity. Second, the detection of drilling problems often lags behind the time frame in which wellbore issues develop. This delay frequently results in a lack of timely responses and, consequently, in a possibly severe deterioration of wellbore conditions before problems are identified.

To address these challenges, various researchers have suggested automating the solids characterization task using sensing devices and computer vision algorithms. These sensing devices fall into two categories: cuttings flowmeters, which measure the weight of the solids stream, and 2D cameras, which capture images of the shale shakers. Both types of devices have limitations. First, cuttings flowmeters require the assumption or manual estimation of the cuttings' density to obtain a volume measurement. Additionally, these devices do not capture sufficient data to distinguish cuttings from cavings, nor can they determine the solids' morphological characteristics.

Second, while 2D cameras capture data that can be used for describing the geometry of solids, field tests of camera-based systems have revealed that the quality of such descriptions is highly dependent on environmental conditions, such as the amount of light, the presence of fog from the evaporation of the drilling fluid, the extent of fluid-solid separation at the shakers, and the fluid opaqueness (Holt and Ruel 2022; Jing et al. 2024). In addition, cameras located at a considerable distance from the shakers may fail to capture sufficient details for the identification and characterization of individual cuttings and their distinction from cavings. Finally, cameras convey limited data for

*Corresponding author; email: abraham.montes@utexas.edu

Copyright © 2024 The Authors.

Published by the Society of Petroleum Engineers. This paper is published under the terms of a Creative Commons Attribution License (CC-BY 4.0)

This paper (SPE 217736) was accepted for presentation at the IADC/SPE International Drilling Conference and Exhibition, Galveston, Texas, USA, 5–7 March 2024, and revised for publication. Original manuscript received for review 17 March 2024. Revised manuscript received for review 15 June 2024. Paper peer approved 8 July 2024. Supplementary materials are available in support of this paper and have been published online under Supplementary Data at https://doi.org/10.2118/217736-PA. SPE is not responsible for the content or functionality of supplementary materials supplied by the authors.



Downloaded from http://onepetro.org/SJ/article-pdf/29/10/5238/3677062/spe-217736-pa.pdf/1 by The University of Texas At Austin user on 30 April 2025

estimating the volume of solids, as the pixels' values in the associated 2D images depend on the color of the reflected light and not exclusively on depth measurement.

Solids' characterization systems that employ 2D cameras primarily rely on a subset of three computer vision tasks, which are image classification, object detection, and segmentation. Image classification has been proposed for the qualitative description of the shakers' load. For instance, Badis et al. (2021) proposed the classification of shakers' images into 14 categories associated with flow rate conditions. The authors used a histogram of oriented gradients feature extractor, and a variety of classifier types, including support vector machine, logistic regression, multilayer perceptron, and random forest. Du et al. (2020) proposed a convolutional neural network (hereinafter abbreviated as CNN) with an adapted VGG-16 architecture for classifying the shakers' load into four categories: none, light, heavy, and extraheavy. More recently, Holt and Ruel (2022) proposed the use of pretrained CNNs for the classification of the shakers' load into 10 categories ranging from "no-flow" to "overflow." Although the model used is not disclosed in their paper, the authors outlined various state-of-the-art CNNs suitable for this task, such as InceptionV3 (Szegedy et al. 2016). Although the categorization of the shakers' loading may be used as indicative of potential drilling problems, it is not sufficient for a complete description of the solids, including volume and morphology. This, in turn, limits these systems' capability to evaluate hole cleaning sufficiency and wellbore stability.

Object detection and segmentation techniques are utilized for the identification of individual solids. Methods that apply these techniques to images of the shakers are scarce. For instance, Badis et al. (2021) used a region-based CNN (R-CNN) to detect individual solids, find their bounding box, and classify them by shape into splintery, angular, and round categories. Grossi et al. (2023) used a U-Net—a type of CNN—for the identification of regions in the shakers' screens occupied by solids. These solutions provide greater detail about the solids' shapes than methods relying solely on image classification. However, they are not sufficient for a comprehensive description of the solids, as they cannot determine the dimensions of individual solids or their volume.

Other authors leverage segmentation and object detection techniques on images of clean, presorted, and dried solids. For instance, Jin et al. (2022) proposed the use of contour- and surface-related features extracted from images of cavings to classify them into four categories associated with distinct rock failure mechanisms, using a boosting-type ensemble model. Nanjo et al. (2023) used a combination of two CNNs to identify the cuttings' lithology. These solutions, however, do not solve the problem of late identification of potential issues, because they rely on manual collection and preparation of the solids, which do not occur in real time.

**Table 1** summarizes previously proposed solutions to solids' characterization and highlights key capabilities required for a comprehensive evaluation of wellbore conditions. Notably, while these devices are suitable for operating in hazardous environments (except for Saasen et al. 2009), none of them offers a complete characterization of cuttings and cavings. In fact, none of these proposed devices can detect, characterize, and classify cavings in real time, which is pivotal for diagnosing potential wellbore instability and forewarning of associated stuck pipe events.

| System Characteristics | Naegel et al. (1998); Thonhauser et al. (1999) | Saasen et al. (2009) | Marana et al. (2010) | Graves and Rowe (2014) | Torrione (2021) | Du et al. (2020) | Badis et al. (2021) | Holt and Ruel (2022) |
|---|---|---|---|---|---|---|---|---|
| Automated system | ✓ | – | ✓ | ✓ | ✓ | ✓ | – | – |
| Type of device | Cuttings flowmeter | Cuttings flowmeter and imaging device | Camera | Charge coupled device camera | Camera | Camera | Camera | Camera |
| Type of data | Cuttings weight | Cuttings weight and 2D images | 2D images | 2D images | 2D images | 2D images | 2D images | 2D images |
| Measures volume of cuttings | ✓ | ✓ | – | ✓ | ✓ | – | – | – |
| Measures size of cuttings | – | ✓ | – | ✓ | ✓ | – | – | – |
| Classifies shape of cuttings/cavings | – | ✓ | – | ✓ | – | – | ✓ | – |
| Detects cavings in real time | – | – | – | – | – | – | ✓ | – |
| Field tested | ✓ | – | ✓ | – | – | ✓ | – | ✓ |
| Operates in any lighting environment | ✓ | – | – | ✓ | ✓ | – | – | ✓ |
| Operational in hazardous locations | ✓ | – | ✓ | ✓ | ✓ | ✓ | – | ✓ |

Key: ✓ = The system possesses the indicated characteristic; – = Either the system lacks the indicated characteristic or the publication does not mention it.

Table 1—Capabilities of previously proposed cuttings/cavings sensors (adapted from Prez et al. 2023).

To fill the identified gaps, our research group developed a laser-based sensor with a Class-1, Division-1 enclosure that provides a comprehensive characterization of the solids stream. This equipment integrates a high-resolution camera and a 3D laser line profile scanner, which enable the simultaneous acquisition of 2D and 3D data (Han et al. 2017, 2018). Recently, this device was upgraded incorporating (1) a conveyor system suitable for hazardous environments and (2) a complete enclosure to ensure a controlled-lighting environment. These improvements have not only enhanced the sensor's accuracy by eliminating environmental noise such as sunlight but have also

Downloaded from http://onepetro.org/SJ/article-pdf/29/10/5238/3677062/spe-217736-pa.pdf/1 by The University of Texas At Austin user on 30 April 2025

enabled precise estimation of the speed of cuttings passing through the sensor. This speed estimation is crucial for accurately deriving the morphological description of solids from the acquired data (Prez et al. 2023). **Fig. 1** provides an illustration of the key components of this sensor and its configuration. In the subsequent paragraphs, we will delve into the methods for identifying cuttings/cavings and inferring their morphological characteristics and volume.

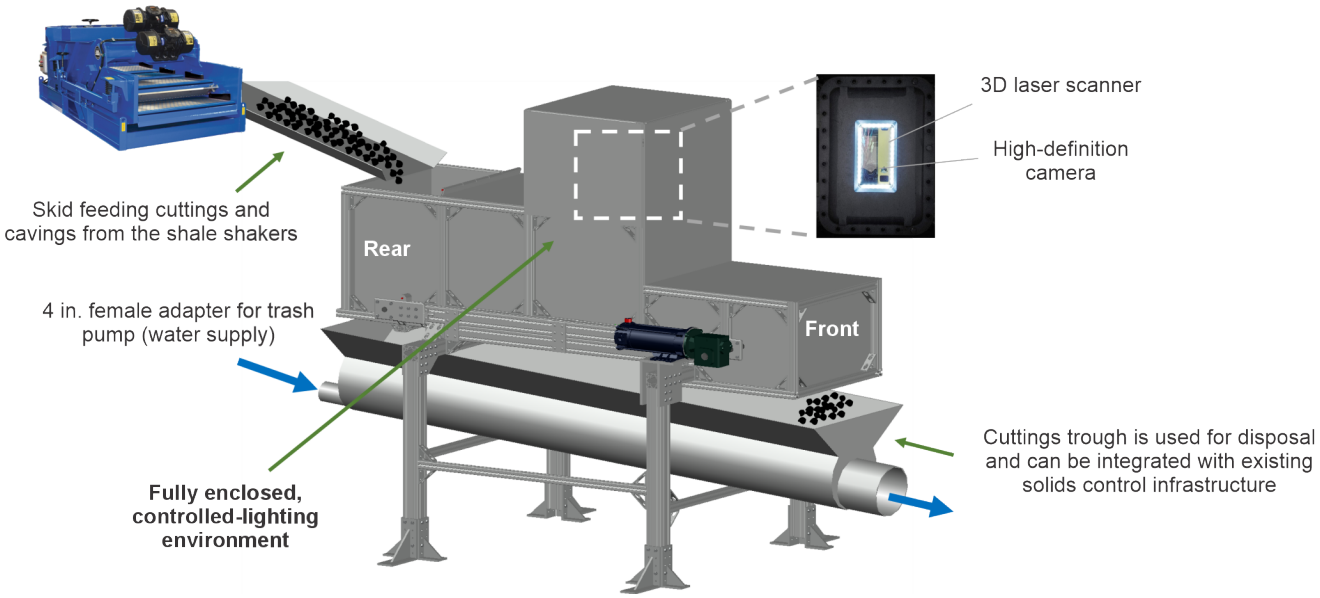



**Fig. 1—Schematic of the fully enclosed laser-based sensor developed by our research group at The University of Texas at Austin (after Prez et al. 2023).**

Han et al. (2018) proposed an initial method to identify and characterize cuttings and cavings by employing the data collected with the sensor (3D point-cloud data and 2D images). This method relied on image processing techniques, such as edge detection and planes segmentation algorithms. Initial tests of this method in a laboratory environment, as well as preliminary yard trials, showed that it enabled the detection of cavings with an accuracy of 90%. Moreover, it enabled their morphological classification with 75% accuracy. However, this method relied on ideal scenarios such as dry cuttings and cavings and approximately sparse arrangements of these cuttings and cavings. Although these scenarios occur in drilling operations, it is not uncommon to observe wet cuttings/cavings (with drilling mud) and stacked arrangements (Moore 1986).

Han et al. (2018) also proposed a method for estimating the volume of the cuttings/cavings stream by numerically integrating the laser-generated profile associated with such a stream. This method was recently validated in a field test (Prez et al. 2023). This test took place while drilling a slimhole section (6 1/8 in.) with oil-based mud in a well in west Texas, USA. The analysis of the field test revealed that the estimated volume of the returning cuttings was closely aligned with the results of a transient cuttings transport simulation, with only a minor discrepancy noted. The authors attributed this minor discrepancy to a potentially varying void ratio in the sample. This void ratio corresponds to the fraction of the estimated volume that is not associated with cuttings/cavings. In the method used in the field test, this void ratio was assumed to be constant, according to empirical studies available in the literature. Although this approach produces accurate-enough results when the cuttings/cavings have approximately similar sizes and shapes, such as in the case of the field test, it may lead to significant errors in other, more common scenarios where drilling solids are not homogeneous.

In this paper, we propose an enhanced method that leverages both 2D and 3D data acquired with the sensor depicted in **Fig. 1**. This method addresses the limitations identified in previously introduced methods. It not only enables an accurate characterization of cuttings and cavings, even in circumstances when they are stacked, mud-wet, and/or highly heterogeneous in terms of size and shape, but, in addition, it uses such a characterization to accurately estimate the void ratio. This, in turn, enables an accurate and robust estimation of the solids volume. Moreover, our method is not limited to cases where the drilling fluid and the cuttings/cavings expose color contrast. It leverages image processing techniques, state-of-the-art computer vision techniques, such as deep CNNs, and 3D data to overcome challenges associated with low-contrast conditions.

The remainder of this paper is organized as follows. First, we outline the fundamental principles of our method. Next, we delve into each component, including (1) the identification of mud-wetting, (2) identification of individual cuttings/cavings (segmentation), (3) extraction of their size/shape, and (4) estimation of the volume correction factor—which depends on the void ratio. Subsequently, we describe the laboratory experiments that were conducted to gain a deeper understanding of the relationship between the morphological characteristics of the cuttings/cavings and the volume correction factor. Finally, we present the conclusions of our work and future steps to integrate the featured device and proposed method into fully automated NPT prevention systems.

## Method for Cuttings and Cavings Characterization

The proposed method consists of three primary workflows, as illustrated in **Fig. 2**. The first workflow focuses on the morphological characterization of cuttings/cavings in terms of their size and shape. The second workflow is dedicated to estimating the volume of solids in the stream. The third and last workflow assesses the wellbore condition in terms of hole cleaning sufficiency and wellbore stability. Each workflow receives different types of input, including 2D images, 3D data, and cuttings transport simulations. However, the ultimate goal of our method, which is the assessment of the wellbore condition, combines the outputs of the three workflows.

The cuttings/cavings characterization workflow relies on the semantic segmentation of 2D and 3D data. This forms the foundation of the method because identifying each cutting or caving in the images is crucial for their subsequent characterization. Subsequently, the



Downloaded from http://onepetro.org/SJ/article-pdf/29/10/5238/3677062/spe-217736-pa.pdf/1 by The University of Texas At Austin user on 30 April 2025

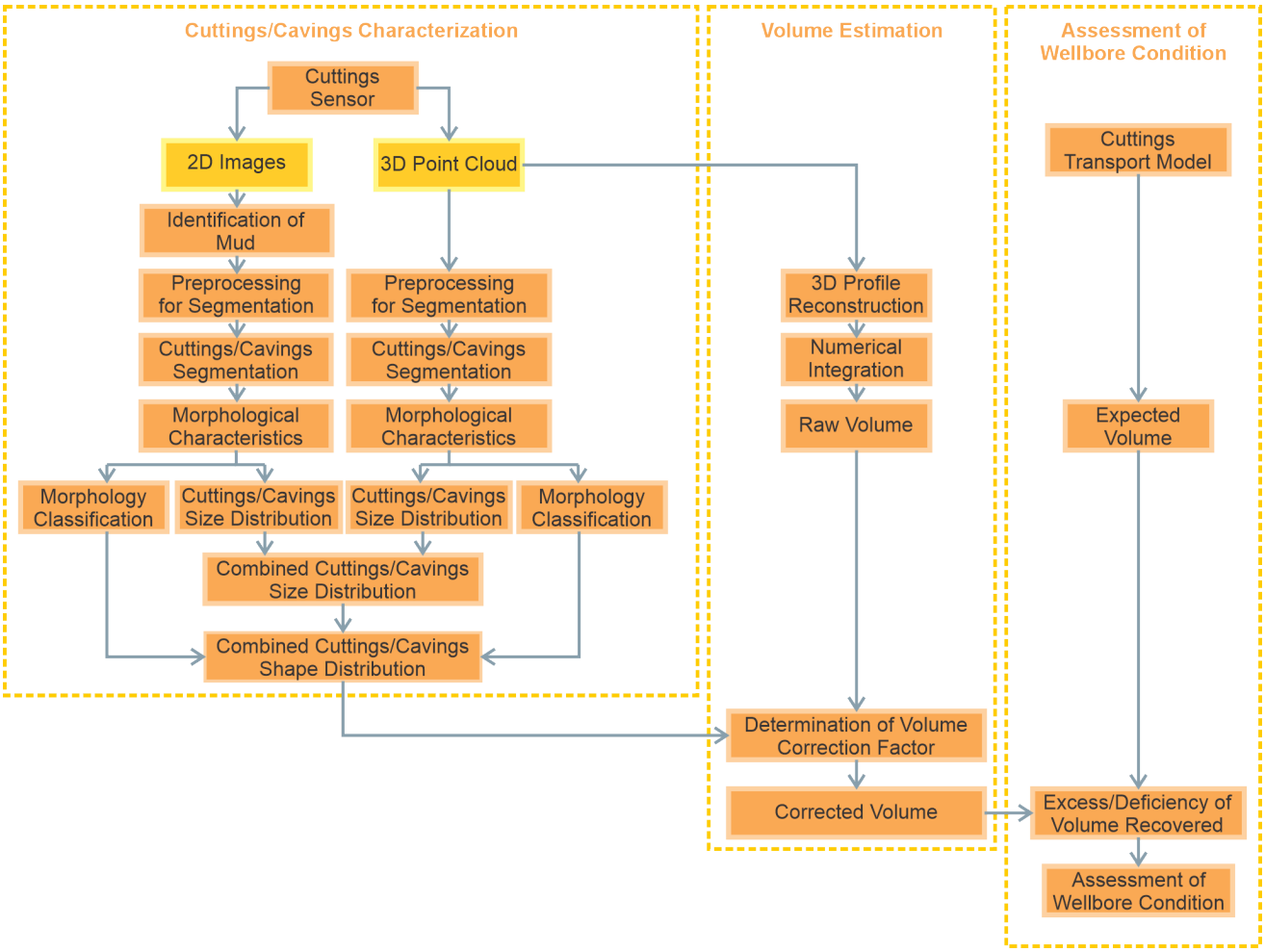



**Fig. 2—Cuttings/cavings characterization and volume measurement workflow.**

workflow involves extracting and processing morphological features related to these segmented cuttings/cavings. This encompasses not only their size and shape but also important features for their later classification, such as angularity and eccentricity (detailed explanations of these features are given in a later section). Finally, the resulting size and shape distributions from both the 2D and 3D branches are combined to determine the necessary correction to the raw volume.

The volume data are obtained from the 3D point cloud data (hereinafter abbreviated as PCD) through a two-step process: The reconstruction of the 3D profile of the sample passing through the laser scanner and the numerical integration of these profiles along the belt-movement axis. This integration of the profiles provides the initial volume of cuttings streamed through the equipment, as illustrated in **Fig. 3**. To ensure accuracy, this raw volume is subsequently adjusted to account for the sample void ratio, which considers the empty spaces between stacked cuttings. This adjustment is based on the sample size distribution and shape, and, consequently, requires the output of the cuttings/cavings characterization workflow.

In addition to enabling the estimation of the samples' void ratio, the first workflow also involves the identification and description of cavings. Accurate detection and morphological description of cavings are essential for the timely recognition of wellbore instability issues. Our method employs two approaches for this purpose. The first approach involves panoptic segmentation of 2D and PCD-based images. This segmentation, performed concurrently with cuttings segmentation, distinguishes individual cavings from the underlying amorphous bed of cuttings. Through panoptic segmentation, we extract information about caving size and shape, as well as the cuttings-to-cavings ratio, which is then used to estimate their volume. The second approach involves the use of morphological descriptors of individual cavings, such as their angularity and eccentricity, and an ensemble classifier, to classify each caving into one of four classes. We will further detail these approaches in a later section.

Finally, our method compares the corrected volume, measured with the sensor, with the expected volume according to a cuttings transport model. This comparison, which yields the excess or deficiency of the returning volume of solids, can be combined with the volume and characteristics of cavings to evaluate hole cleaning sufficiency and wellbore stability. Ultimately, this enhances decision-making around drilling incidents that originate with poor hole cleaning and wellbore instability, such as stuck pipe events. We will now elaborate on the key components of our methodology.

**Mud-Wetting Identification.** The first step in the cuttings/cavings characterization workflow is the identification of the presence of mud. During this step, we classify the condition of the belt into one of four possible scenarios, as illustrated in **Fig. 4**. This step is fundamental as it helps minimize errors associated with the identification of spurious cuttings (false positives). This situation may occur when the belt is devoid of cuttings/cavings but contains mud stains, as shown in **Fig. 4b**.

Downloaded from http://onepetro.org/SJ/article-pdf/29/10/5238/3677062/spe-217736-pa.pdf/1 by The University of Texas At Austin user on 30 April 2025

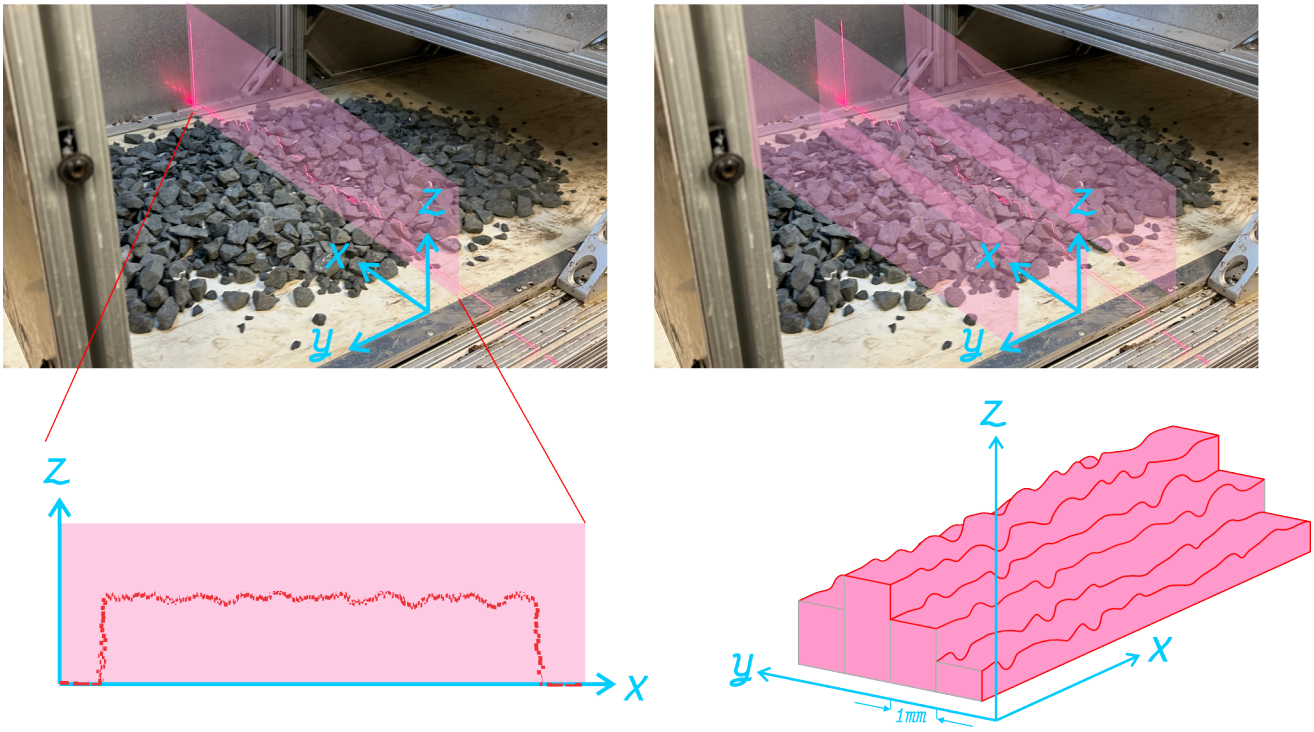



**Fig. 3—Use of the 3D data to obtain an initial estimation of the solids' volume by integrating the reconstructed solids' profile. Each profile is assumed to remain constant for a distance of 1 mm. The volume associated with each profile reading is calculated as the area under the profile multiplied by 1 mm. Finally, the total volume is obtained by summing up the estimated volumes from all profile readings.**

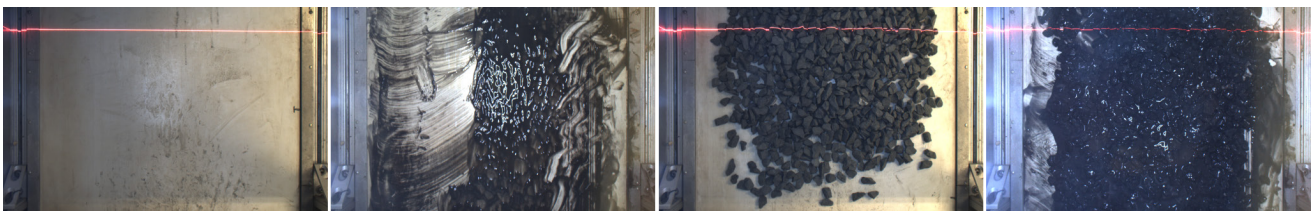


**Fig. 4—Belt conditions associated with the presence of mud—from the left: (a) empty belt, (b) empty belt with mud, (c) dry cuttings, and (d) excessively mud-wet cuttings.**

Additionally, this step plays a key role in determining how to combine 2D- and 3D-based characterizations of cuttings and cavings. Characterizing samples with mud content requires giving emphasis to the 3D-based size and shape distributions, while dry samples can rely on 2D images. This is because 3D data provide essential information, such as the height ($z$-coordinates) of the points, enabling the removal of noise from the data, such as mud stains. We will further explore this point in the upcoming sections.

Finally, this step enables the correct identification of cuttings when these are embedded in the mud **(Fig. 4d)** and reduces outliers associated with the reflections of the laser and the sensor's internal light on the mud.

For this task, we used a pretrained VGG-16 CNN model (Simonyan and Zisserman 2015). We truncated this model at its classification stage (composed of fully connected layers), retaining its feature-extraction part (composed of convolution and subsampling layers). This feature-extraction part, which produces a compressed representation of the image, is commonly known as the "backbone."

To this backbone, we added a random forest model responsible for classifying the compressed representation into one of the four possible belt conditions previously described in **Fig. 4**. The inclusion of the random forest model, instead of the original fully connected layers, resulted in a reduction in the number of training parameters. Specifically, the random forest classifier employs 99.9% fewer parameters than the fully connected layers. This reduction in parameters is evident when comparing the number of trainable parameters in both models: 123,642,856 for the fully connected layers, which include weights and bias terms, vs. 6,520 for the random forest, consisting of the number of variables used for binary splitting at each nonleaf node and the number of thresholds for each splitting. Importantly, this reduction in the number of trainable parameters offers two key advantages: (1) It enables the model to achieve high accuracy even with a limited number of training samples and (2) it reduces computational expenses. **Fig. 5** illustrates the structure of this model.

The random forest classifier also provides confidence levels for each classification of the belt condition, determined by averaging the class probability estimates of each tree in the ensemble. Because our training data set did not include images of partially wetted samples, it is reasonable to interpret this classification confidence level as a proxy for the mud content. We use this mud-content proxy to combine the outputs of the 2D and 3D branches of our workflow. Such a combination involves a weighted sum of the resulting size and shape distributions, where the weights correspond to the estimated mud content—the classification confidence level. The objective is to place



Downloaded from http://onepetro.org/SJ/article-pdf/29/10/5238/3677062/spe-217736-pa.pdf/1 by The University of Texas At Austin user on 30 April 2025

greater reliance on the 3D data in determining the final size and shape distributions when the sample is mud-wetted, as explained earlier in this section. A more detailed discussion of the rationale behind this combination is presented at the end of the subsequent section.

The testing of this model demonstrated exceptional classification performance. It accurately identified 100% of cases involving dry cuttings and a dry/empty belt. For scenarios with wet cuttings and a wet/empty belt, the model achieved an accuracy of 98% and 95%, respectively. These results are summarized in **Table 2**.

| Predicted→ / Actual↓ | Dry Cuttings | Dry Empty Belt | Wet Cuttings | Wet Empty Belt |
|---|---|---|---|---|
| Dry cuttings | 74 | 0 | 0 | 0 |
| Dry empty belt | 0 | 59 | 0 | 0 |
| Wet cuttings | 0 | 0 | 130 | 2 |
| Wet empty belt | 0 | 0 | 2 | 35 |

Table 2—Test results of the proposed mud-wetting identification model (confusion matrix).

**Segmentation of High-Resolution Images and Point-Cloud Data.** The segmentation of 2D images and 3D PCD corresponding to rock fragments has been studied in other fields, such as mining (Andersson et al. 2012; Thurley 2013), aerospace engineering (Di et al. 2013), and civil engineering (Guo et al. 2022). However, the segmentation of images of cuttings and cavings poses a more complex task. This complexity arises from the diverse arrangements of returning solids streams encountered in drilling operations. A model trained for the segmentation of images of cuttings and cavings must exhibit robustness to handle various factors, including (1) different spatial distributions, ranging from sparse to stacked cuttings/cavings; (2) varying mud content in the sample; and (3) variations in the uniformity of the solids stream concerning size and shape. **Table 3** provides a summary of some of these conditions and their potential causes [based on Moore (1986) and Murchinson (1982)].

Aiming to reproduce such a diversity of conditions, we collected and configured various samples, as illustrated in **Fig. 6**. As this figure shows, the samples comprise various combinations of spatial distributions, mud content, and uniformity, including extreme conditions associated with highly stacked cuttings and excessive mud content. In the upcoming section (validation at laboratory scale), we will extend the description of these samples, including their size range, their volume, and the characteristics of the mud.

These samples were processed through the sensor, which yielded data sets of 2D images and 3D PCD. The latter, which consisted of the *x*-*y*-*z* coordinates of points in the Euclidian space (as illustrated in **Fig. 7**), were converted into 2D images through rasterization. In these images, each point is represented as a unique pixel. It is important to note that although the 3D data are represented as rasterized images, such images retain most of the spatial information of the original 3D data. This is because the color channel in these images is exclusively related to the *z*-coordinates of the PCD. Additionally, the point cloud corresponds to the surface of the solids' stream and is uniformly distributed over the *x*- and *y*-directions. As a result, even points representing the edges of a solid are not collapsed into the same pixel in the rasterized image.

| Conditions of Returning Solids | Possible Immediate Causes | Possible Associated Operational Conditions |
|---|---|---|
| Stacked cuttings | High flow out of cavings | • Wellbore instability<br>• Intensive reaming or underreaming operation<br>• Return of an effective high-viscous batch |
| | High flow out of cuttings | • Drilling a section with large hole diameter<br>• High rate of penetration |
| | Equipment failure/maintenance | • Shale shaker(s) out of order<br>• Partial plugging at the shakers' distribution box |
| Mud-wetted cuttings | Incorrect selection/setup of shale shakers | • Mesh openings are too small (mesh size is higher than required)<br>• Unbalanced motion on the shakers' deck (elliptical motion of cuttings and cavings)<br>• Wire coating (obstruction of mesh openings with high-surface-tension liquid) |
| | Improper drilling parameters | • Excessive flow rate |
| | Increased plastic viscosity | • Excessive concentration of low-gravity solids in the fluid<br>• Cooling of the fluid (e.g., during maintenance operations) |
| Poor sorting (wide range of sizes) | Heterogeneous cavings | • Drilling conglomerates<br>• Underreaming while drilling<br>• Induced wellbore instability |
| | Heterogeneous cuttings | • Use of stabilizers with cutters<br>• Use of hybrid bits |

Table 3—Operational conditions associated with various arrangements of cuttings and cavings after passing through the shale shakers.

Downloaded from http://onepetro.org/SJ/article-pdf/29/10/5238/3677062/spe-217736-pa.pdf/1 by The University of Texas At Austin user on 30 April 2025

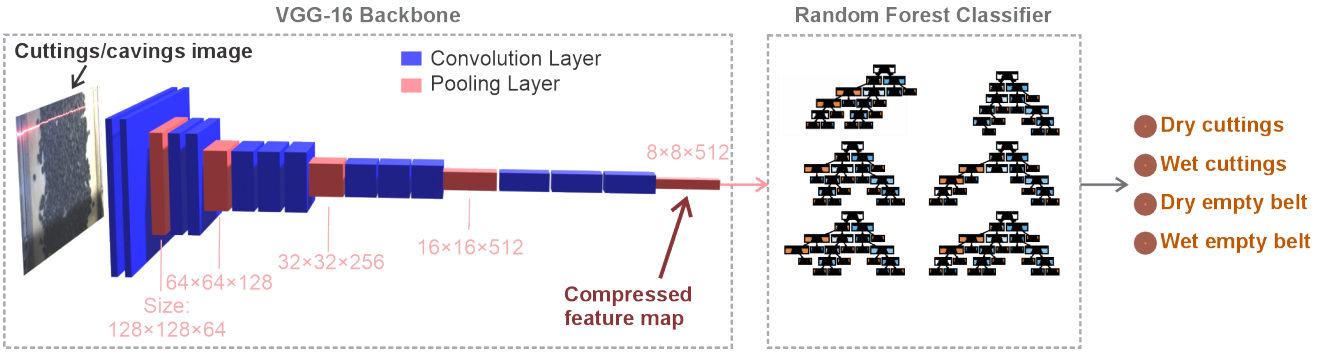



**Fig. 5—Mud-wetting identification model. This model integrates a VGG-16 architecture to extract a compressed representation of the images. Then, it incorporates a random forest classifier to distinguish between four classes: dry cuttings, wet cuttings, dry empty belt, and wet empty belt.**

As can be observed in **Fig. 7**, the raw, unprocessed point cloud data belong not only to cuttings and cavings but also to the metallic frame on the sides of the belt, the minor—but existent—irregularities of the belt, and mud stains. In addition, without any preprocessing, cuttings and cavings are not easily distinguishable from each other when they are stacked. Both types of images (2D and PCD-based images) were high resolution, with 2D images having a 1,920×1,200 pixels resolution and the 3D PCD a point spacing of 1 point/mm.

Although these resolutions are advantageous for accurately identifying individual cuttings and cavings, these images were further enhanced with preprocessing techniques to ensure an accurate segmentation. These preprocessing techniques included image denoising, histogram equalization, image thresholding, and morphological optimization. The application of these techniques not only accentuates the sections of the images corresponding to individual cuttings and cavings but also helps deemphasize the regions that are not of interest (e.g., sections of empty belt, mud stains on the belt, and the metallic frame). Additionally, these preprocessing techniques are key to avoiding erroneous segmentation under poor sorting scenarios (Guo et al. 2022). **Fig. 8** illustrates these beneficial adjustments on 2D and PCD-based images of stacked cuttings.

Each of these preprocessing techniques requires the definition of several parameters. For instance, the histogram equalization process can be carried out globally (for the entire image) or locally. The latter case involves a rectangular moving window in which the

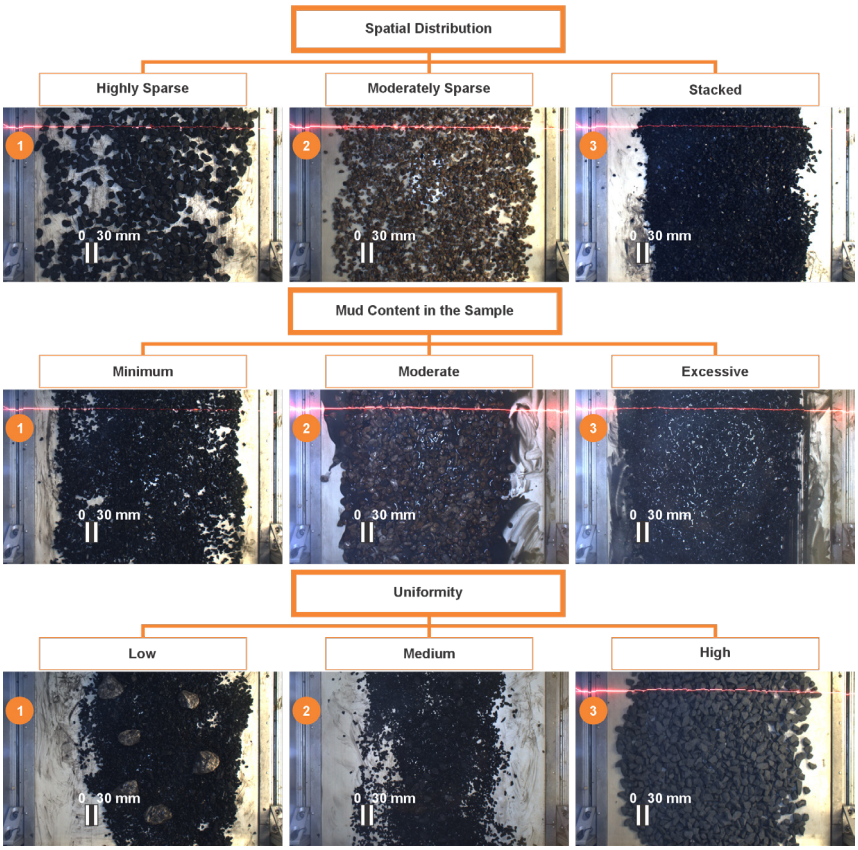



**Fig. 6—Characteristics of solids arrangements used in the development of segmentation models. Top: different spatial distributions of cuttings on the conveyor belt. Middle: different amounts of mud in the sample. Bottom: levels of uniformity in terms of size and shape of cuttings/cavings.**

Downloaded from http://onepetro.org/SJ/article-pdf/29/10/5238/3677062/spe-217736-pa.pdf/1 by The University of Texas At Austin user on 30 April 2025

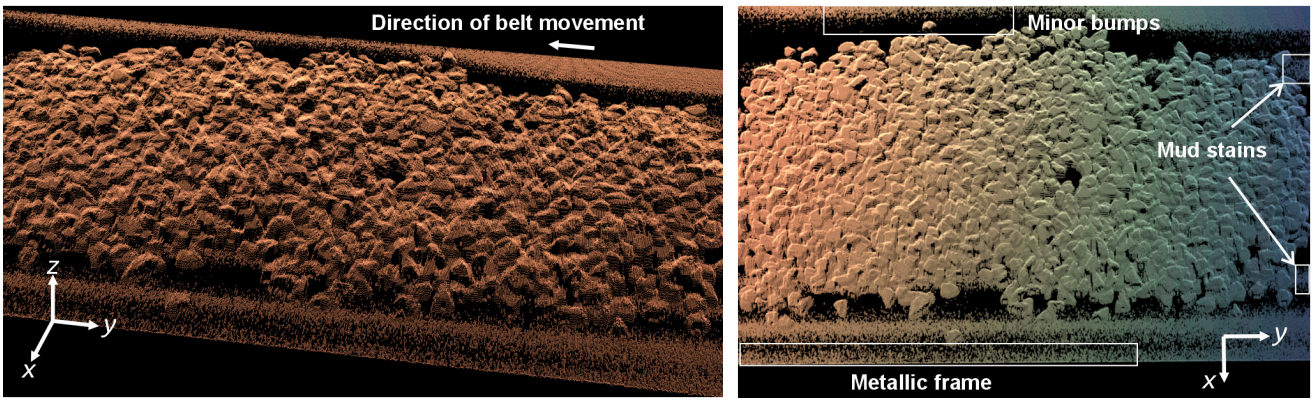



**Fig. 7—3D images obtained with the point cloud data. Left: Point cloud data corresponding to stacked angular cuttings. Right: Top view of the same cuttings stream.**

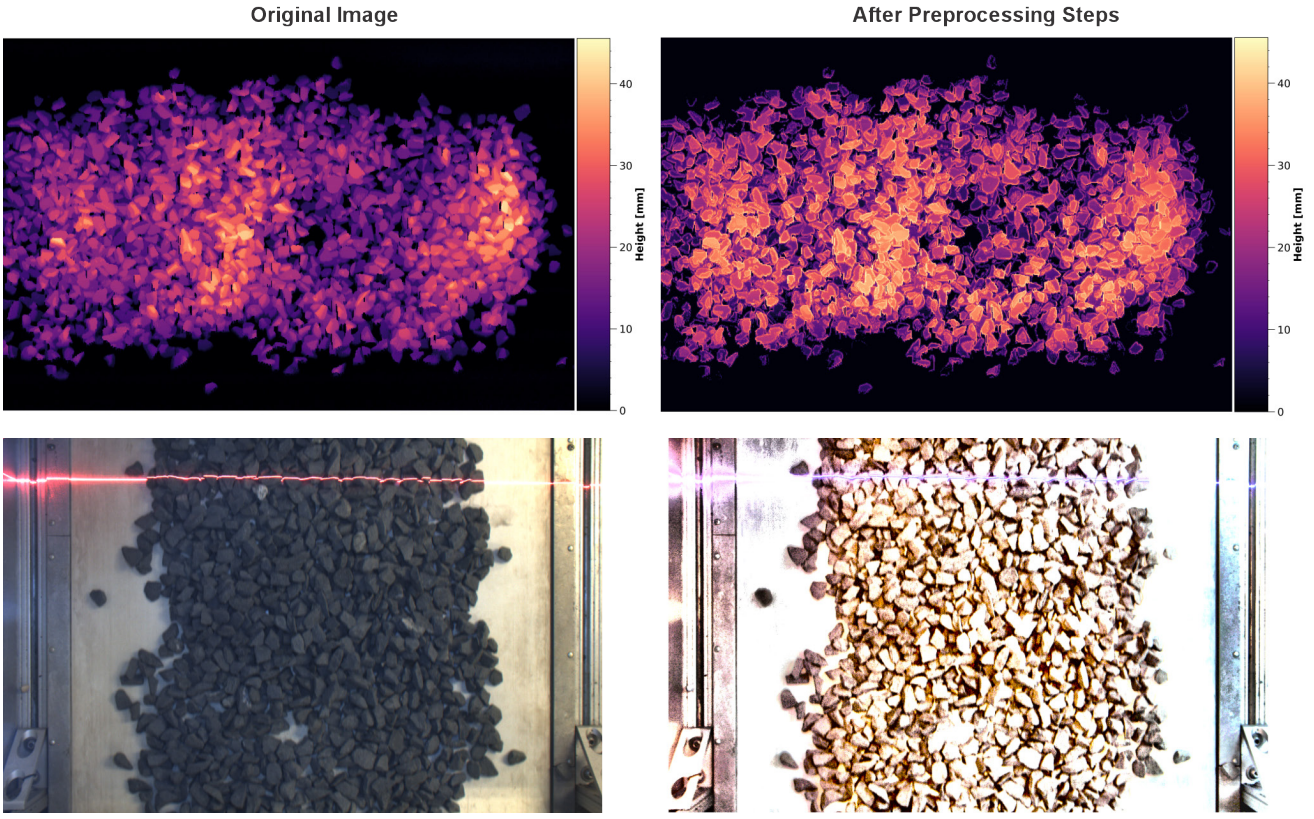



**Fig. 8—Image enhancement with preprocessing techniques before being fed into segmentation models. Top: PCD-based images, where the color represents the height dimension. Bottom: 2D images obtained with the camera. The images on the left correspond to the unprocessed data. The images on the right show the effect of the preprocessing steps on the data.**

equalization is performed separately on different regions of the image. In such a case, the algorithm requires the size of the moving window and a contrast transformation limit.

It is worth noting that, as each preprocessing method involves numerous parameters, there is a vast number of possible combinations. The process of finding the optimal combination is nontrivial. The search space in this optimization problem becomes so large that exhaustive, uninformed search techniques would demand an unreasonable amount of time. To tackle this problem, we implemented a genetic algorithm that accelerates the search for the optimal combination of parameters by implementing a metaheuristic. We encourage interested readers to refer to the supplementary material of this paper for a detailed description of the algorithm.

After preprocessing the data with optimized methods, we proceeded to investigate the suitability of various segmentation techniques. These techniques included (1) hierarchical density-based spatial clustering of applications with noise (HDBSCAN) (Campello et al. 2013; Wang et al. 2023), (2) the watershed algorithm (Chen et al. 2004; Guo et al. 2022), (3) convolutional autoencoders (U-net architecture; Ronneberger et al. 2015) and the Segment Anything Model (Kirillov et al. 2023), and (4) a mask R-CNN (He et al. 2020). The selection of these methods relied not only on the literature on applications of computer vision across multiple domains but also on rankings in established image segmentation competitions, such as the Common Objects in Context and Large Vocabulary Instance Segmentation challenges (Gupta et al. 2019).



Downloaded from http://onepetro.org/SJ/article-pdf/29/10/5238/3677062/spe-217736-pa.pdf/1 by The University of Texas At Austin user on 30 April 2025

These segmentation models were compared based on the resulting estimation of the cuttings/cavings size distribution. The methodology to carry out such an estimation is described in the upcoming section. **Table 4** summarizes the effectiveness of each model under various possible scenarios of the cuttings/cavings stream. This effectiveness was determined based on the fidelity of the estimated size distribution. Additionally, the table outlines the model's real-time capabilities, a crucial feature for timely wellbore condition assessment.

| | | Sample Characteristics† | | | | | | | | | |
|---|---|---|---|---|---|---|---|---|---|---|---|
| | | Spatial Distribution | | | Mud Content | | | Uniformity | | | |
| Segmentation Model | Type of Data* | 1 | 2 | 3 | 1 | 2 | 3 | 1 | 2 | 3 | Real-Time Applicability |
| Hierarchical density-based spatial clustering | 3D | ✓ | – | – | ✓ | – | – | – | – | ✓ | Yes |
| Enhanced watershed | 2D, 3D | ✓ | ✓ | – | ✓ | – | – | ✓ | ✓ | ✓ | Yes |
| Convolutional autoencoders | 2D, 3D | ✓ | ✓ | ✓ | ✓ | ✓ | – | ✓ | ✓ | ✓ | No |
| Region-based CNN | 2D, 3D | ✓ | ✓ | ✓ | ✓ | ✓ | ✓ | ✓ | ✓ | ✓ | Yes |

Keys: ✓ = The segmentation model can identify a representative number of solids without spurious or incorrect predictions under the indicated sample conditions. – = The segmentation model does not identify a representative number of solids and/or predicts spurious solids.

*Indicates the type of data used in the experiments to determine the applicability of each segmentation model. When 2D and 3D are specified, these types of data were used on separate experiments and the concluded applicability was the same.
†Refer to Fig. 6 to associate the indicated numbers with examples of the samples' characteristics.

Table 4—Applicability of segmentation models to various arrangements of returning cuttings and cavings.

**Table 4** shows that the mask R-CNN model not only excels in accurate segmentation of individual cuttings and cavings under all tested conditions but also operates in real time. Notable features of this model include the following:

- It implements a training method (fast R-CNN) specially designed to optimize the required time for training and for generating predictions (Girshick 2015). This characteristic enables the real-time morphological description of individual cuttings and cavings, which, in turn, is used to assess the wellbore condition in a timely manner.
- Multiple mask R-CNN models pretrained on extensive reference data sets like Common Objects in Context and ImageNet are available under free software licenses. These models can be leveraged for transfer learning. In this study, we utilized Detectron2 (Wu et al. 2021), an open-source library that offers a range of pretrained mask R-CNN models. We retrained one of these models using a database consisting of 742 2D and PCD-based images, representing drilled solids with varying size ranges, mud content, and spatial distributions. This resulted in two segmentation models, one for each type of image.

While detailed descriptions of this model and its training algorithm are out of the scope of this paper, we encourage interested readers to consult He et al. (2020) and Girshick (2015) for more information.

**Fig. 9** displays examples of segmented images featuring stacked cuttings with and without mud content. Notably, while the presence of excessive mud content presents a significant challenge, the mask R-CNN model successfully segments a representative subsample of these cuttings. This is evident when comparing the actual and estimated size distributions, as detailed in the upcoming section. Importantly, the model does not misclassify regions of the image corresponding to mud stains or empty belt as cuttings. These regions tend to be amorphous and considerably larger than the cuttings. This avoidance of misclassification enhances the fidelity of the estimated size distribution. This model's accuracy in scenarios with excessive mud content sets it apart as a key differentiating feature compared with the other models in **Table 4**.

Finally, it is worth noting that, in the presence of mud, the segmentation of PCD-based images tends to produce more reliable predictions than that of 2D images. This is primarily because of two reasons. First, the color in 2D images is controlled by the reflection of certain wavelengths of light. Frequently, the reflections from the mud and the cuttings, which affect their visible colors in 2D images, are similar, resulting in a low contrast between them. This low contrast may produce inaccurate or incomplete segmentation results. In PCD-based images, on the other hand, the color is controlled by the height dimension of the PCD, instead of the reflection of certain wavelengths of light. This not only eliminates the problem of low contrast but also facilitates the detection of the borders between adjacent cuttings.

The second reason is related to the effective removal of mud stains with the preprocessing methods. In PCD-based images, these methods often exclude point cloud corresponding to mud stains after applying thresholds in the height dimension. This does not occur in 2D images, where mud stains may remain, especially when these stains are located in the interstitial spaces between cuttings in moderately sparse arrangements.

**Fig. 10** shows a comparison between segmented 2D and PCD-based images of a basalt sample wetted with asphalt-containing water-based mud. As described earlier, the segmentation performance of 2D images decreases with increasing mud content, especially when the mud color is similar to that of the cuttings. In cases of excessive mud content, the morphological characterization of solids will rely entirely on PCD images because the segmentation of 2D images tends to produce abundant spurious, incorrect masks (i.e., the black-and-white representation of each solid) that are often significantly larger than the cuttings. However, when the sample is completely dry, the characterization will rely solely on 2D images due to their higher resolution, which often facilitates the identification of a greater number of solids (see **Fig. 9**). Intermediate cases will use a weighted sum of both characterization results (as detailed in the "Mud-Wetting Identification" section).

**Size Distribution Estimation.** Once the individual cuttings and cavings are identified with the segmentation model, we find the best-fitting ellipses for each of them. Ellipse fitting, which has been previously applied in the morphological description of rocks (Girdner et al. 1996; Di et al. 2013), is an alternative to describe cuttings with real-time applicability. The calculation of these ellipses is made by



Downloaded from http://onepetro.org/SJ/article-pdf/29/10/5238/3677062/spe-217736-pa.pdf/1 by The University of Texas At Austin user on 30 April 2025

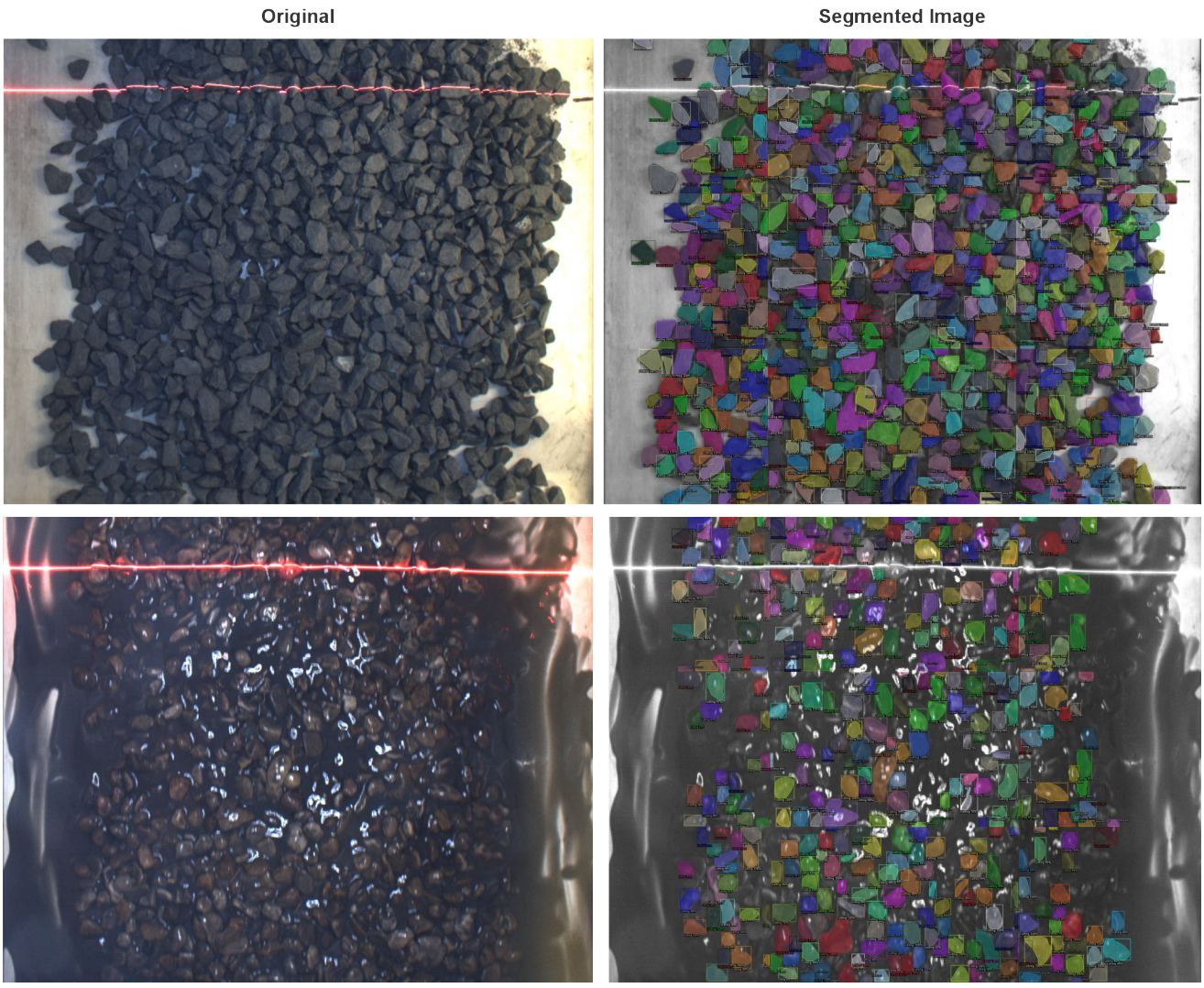



**Fig. 9—Segmentation of images corresponding to stacked cuttings. The top image corresponds to a minimum mud content scenario, while the bottom one corresponds to an excessive amount of mud. The images on the right correspond to the output of the mask R-CNN model. The original images in these examples were divided into nine tiles to increase the speed of the segmentation prediction.**

computing the normalized central moments of the solids' masks. This method, which is not computationally intensive, reduces the risk of overestimating the solids' dimensions, particularly given the irregularity of their boundaries (Mulchrone and Choudhury 2004).

It is worth noting that ellipse fitting is not the only option for extracting the solids' dimensions. Multiple researchers in the mining industry have successfully used box fitting (Wang 2006; Andersson et al. 2012). Although box fitting was evaluated in our application, we found it to be less effective than ellipse fitting. Both techniques tend to slightly underestimate the actual solids' dimensions, but ellipse fitting produces estimates closer to the actual dimensions. Future research will explore other methods for ellipse and box fitting, as well as their application to a wider range of cuttings' lithologies and shapes.

The lengths of the major and minor axes of the best-fitting ellipses, along with their eccentricity, are used as morphological descriptors of the detected solids. We use these lengths to construct the estimated size distributions (i.e., the cuttings length and width distributions, respectively, abbreviated as LD and WD). The eccentricity, on the other hand, is used to describe the resemblance to splinters, as we will describe in the subsequent section.

Additionally, these fitted ellipses also serve as baselines to determine the angularity of cuttings and cavings. In this case, the main descriptor is the existing area between each cutting/caving and their corresponding fitted ellipse. In this sense, rounded cuttings are expected to have smaller cutting-ellipse areas than angular ones, as illustrated in **Fig. 11**.

It is worth noting that, with a clean belt, the segmentation of highly sparse, nonwet samples achieves 100% accuracy. Consequently, the dimensions of the fitted ellipses closely match the actual dimensions of cuttings/cavings. **Fig. 12** illustrates this point. In this particular case, the ground truth (actual size distribution) was determined through manual measurements of the length and width of a large sample of cuttings without mud-wetting. The estimated size distribution, on the other hand, was obtained by (1) segmenting the generated images using the watershed algorithm, (2) fitting ellipses to each solid, and (3) extracting the axis lengths of the fitted ellipses.

Because of its accuracy on sparse, nonwet samples, this method for extracting the size distribution also serves as the foundation for evaluating the effectiveness of segmentation techniques under different arrangements of cuttings/cavings, as mentioned in the previous section. A segmentation technique that accurately identifies individual cuttings or cavings should also yield a high-fidelity size distribution. In summary, the following process was used to assess the effectiveness of a segmentation technique on a specific arrangement of cuttings/cavings:

Downloaded from http://onepetro.org/SJ/article-pdf/29/10/5238/3677062/spe-217736-pa.pdf/1 by The University of Texas At Austin user on 30 April 2025

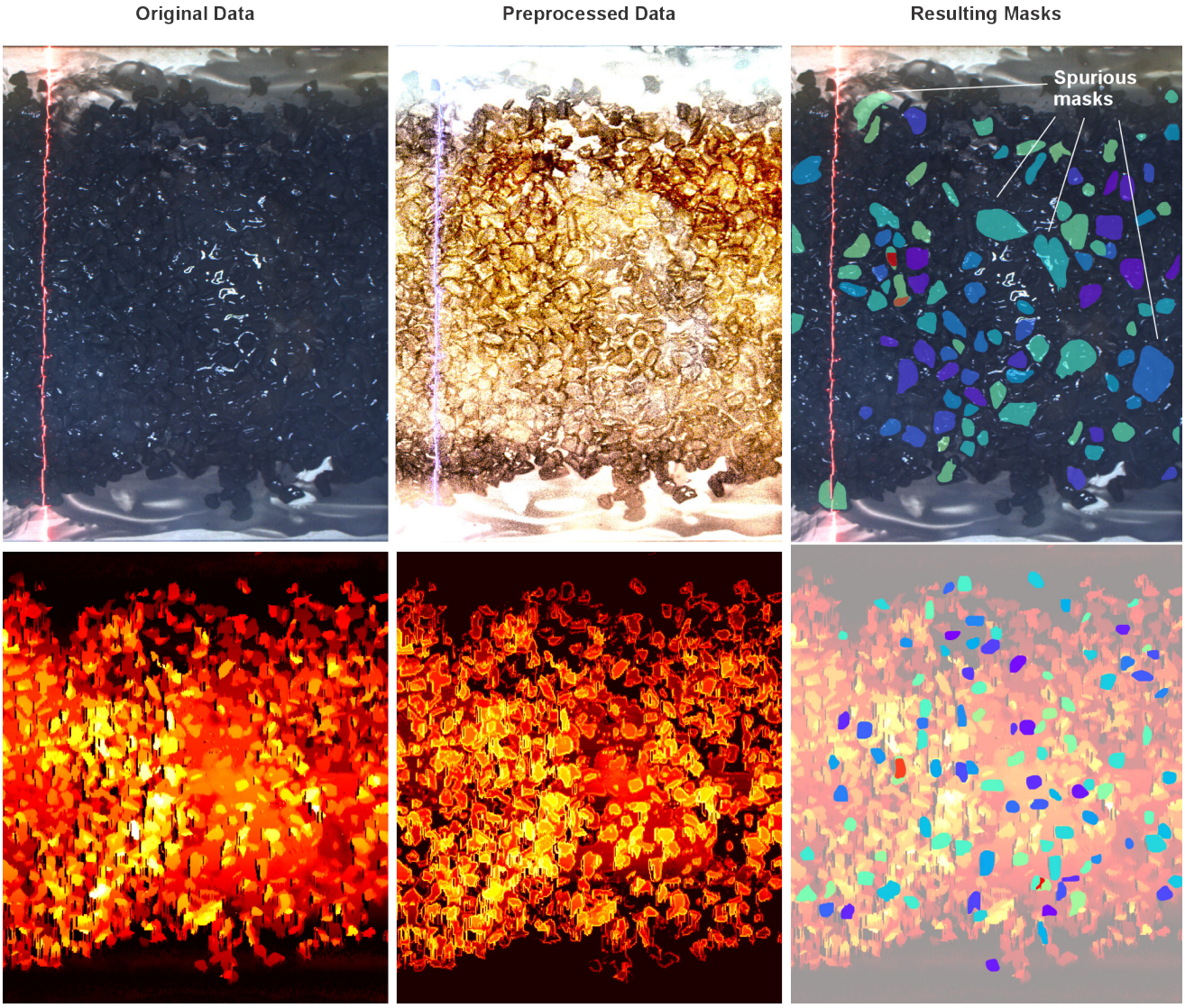



**Fig. 10—Comparison between segmentation of 2D and PCD-based images in a sample with excessive mud content and low color contrast. Despite the use of preprocessing techniques, segmentation of the 2D image results in multiple spurious masks (top). In contrast, segmentation of PCD-based images results in a representative number of correctly predicted masks (bottom).**

1. Collect the sample with minimum mud content.
2. Distribute the sample on the conveyor belt in a sparse manner and collect the associated 2D and 3D data with the sensor.
3. Preprocess and segment the data with the watershed algorithm.
4. Estimate the actual size distributions ($LD_{actual}$ and $WD_{actual}$) by fitting ellipses to each individual cutting/caving and extracting their axes' lengths.
5. Rearrange the sample with specific mud content and spatial arrangement of interest, and collect the associated 2D and 3D data with the sensor.
6. Preprocess and segment the data with the technique of interest (e.g., mask R-CNN).
7. Estimate the size distribution ($LD_{estimated}$ and $WD_{estimated}$) by fitting ellipses to each individual cutting/caving and extracting their axes' lengths.
8. Compare the actual and estimated distributions by calculating the Bhattacharyya coefficient. This coefficient ranges from 0 to 1, where 0 represents completely disjoint, nonoverlapping distributions, and 1 represents identical distributions. A coefficient close to 1 indicates a high-fidelity size distribution and, hence, an accurate segmentation model.

**Fig. 13** shows the size distributions from a stacked, nonuniform sample of cuttings and cavings with excessive mud content. The actual distributions were estimated with the previously introduced procedure. The estimated distributions were derived with the mask R-CNN model and ellipse fitting. It is worth noting that even under these challenging conditions, which is considered an infrequent, worst-case scenario, the proposed method results in fairly good estimates of the size distributions. The similarity scores between the actual and estimated distributions, measured using the previously described Bhattacharyya coefficient, are 0.87 and 0.92 for length and width, respectively. For reference, the similarity score for the distributions in **Fig. 12** is 0.96.

**Cavings Identification and Classification.** Differentiating cavings from cuttings in the returning solids stream is a fundamental step in the assessment of the wellbore stability. Specifically, this assessment requires three inputs: (1) the volume of returning cavings, (2) the classification of these cavings according to their shapes, and (3) the size distribution of cavings. It is worth noting that segmentation

Downloaded from http://onepetro.org/SJ/article-pdf/29/10/5238/3677062/spe-217736-pa.pdf/1 by The University of Texas At Austin user on 30 April 2025

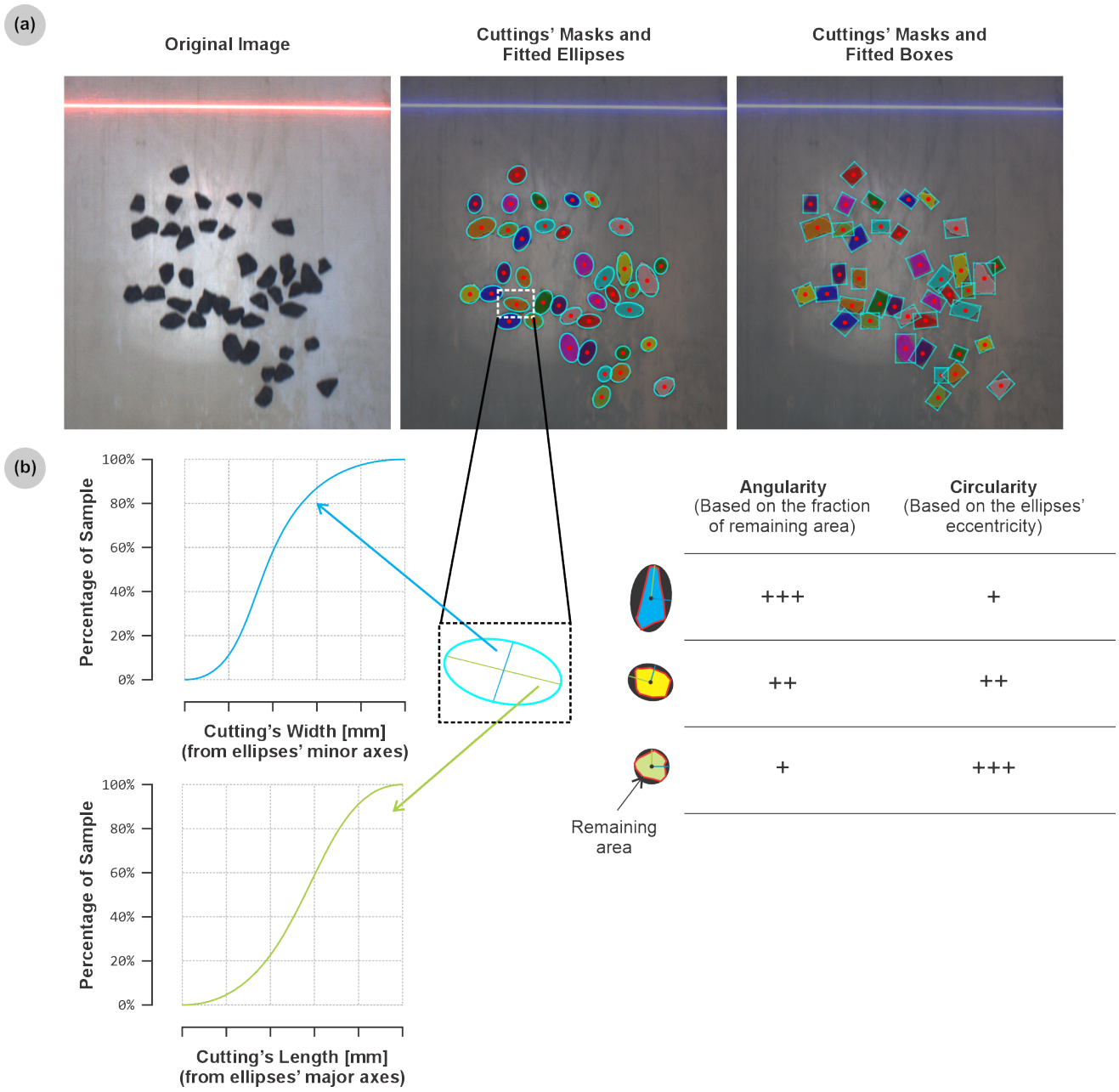



**Fig. 11—(a) Representation of cuttings with fitted ellipses and boxes after image segmentation. (b) Extraction of cuttings' size distribution based on the fitted ellipses. This distribution is divided into width and length distributions. The area between the fitted ellipses and the cuttings is used as a morphological descriptor of cuttings angularity. The ellipses' eccentricity is used to describe the cuttings circularity.**

models can serve this purpose. However, in addition to identifying individual cavings, it is necessary to determine the volumetric ratio of cavings to cuttings.

To estimate such a ratio, we used panoptic segmentation of the recorded images. This type of segmentation combines the identification of individual cavings (instance segmentation) with the delineation of the amorphous, subjacent region that corresponds to the cuttings bed (semantic segmentation). For this purpose, we implemented transfer learning with a pretrained feature pyramid network (FPN) from the Detectron2 library. This network was extended to perform panoptic segmentation of the images from the cuttings/cavings stream passing through the sensor, as illustrated in **Fig. 14**. While a detailed description of this model is out of the scope of this paper, interested readers are encouraged to consult Kirillov et al. (2019) and Lin et al. (2017) for additional information.

Following this panoptic segmentation, we estimated the areas in the images corresponding to cuttings and cavings and took their ratio as an initial surrogate of the cavings-to-cuttings ratio. This estimated ratio was then multiplied by the estimated overall volume to derive the volumetric rate of cavings passing through the sensor, yielding a cavings volume estimate. This overall volume was estimated by numerically integrating the laser-measured profile, as described in previous sections.

In addition to the estimation of the cavings-to-cuttings ratio, the panoptic segmentation model was extended to classify each caving into commonly used morphological classes (as illustrated in **Fig. 14b**). The proportion of these classes, namely, (1) angular, (2) tabular, (3) splintery, and (4) reworked, is commonly used to diagnose the wellbore condition. For instance, angular and splintery cavings are typically associated with low mud density. While angular cavings are generated after the shear failure of the borehole wall, splintery



Downloaded from http://onepetro.org/SJ/article-pdf/29/10/5238/3677062/spe-217736-pa.pdf/1 by The University of Texas At Austin user on 30 April 2025

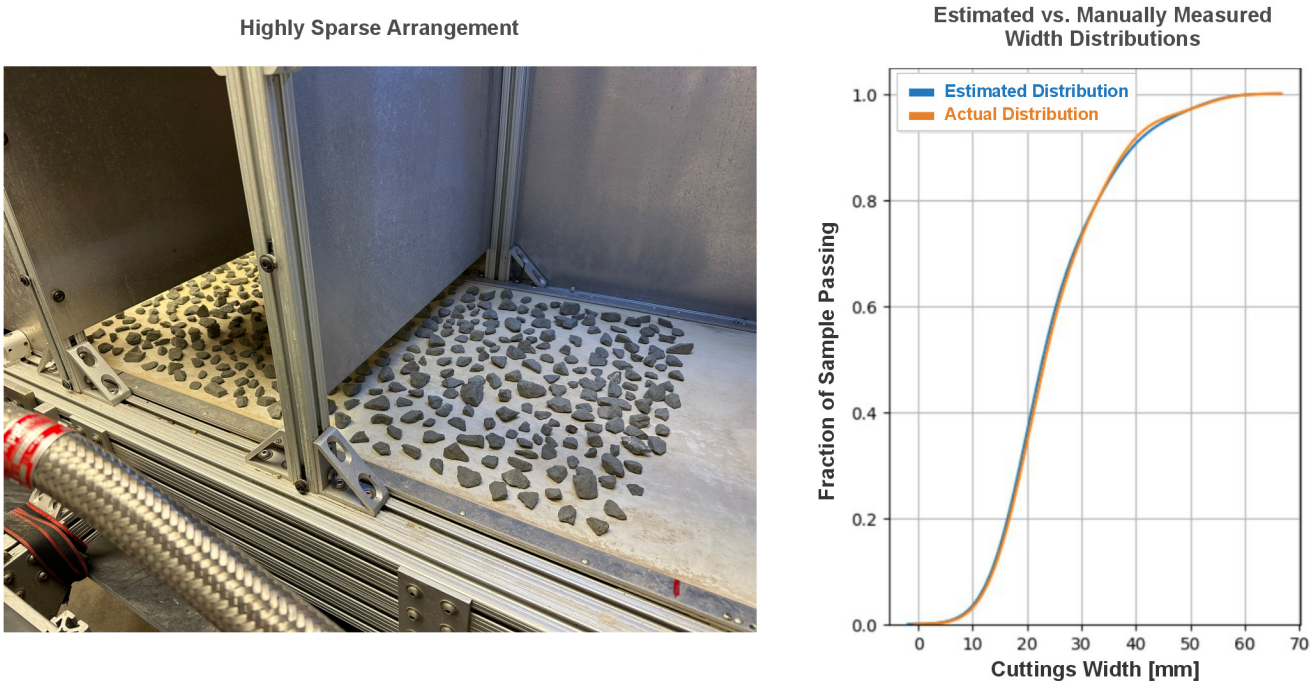



**Fig. 12—Comparison between manually measured and estimated width distributions from a highly sparse, dry sample. The estimated size distribution was extracted by implementing ellipse fitting.**

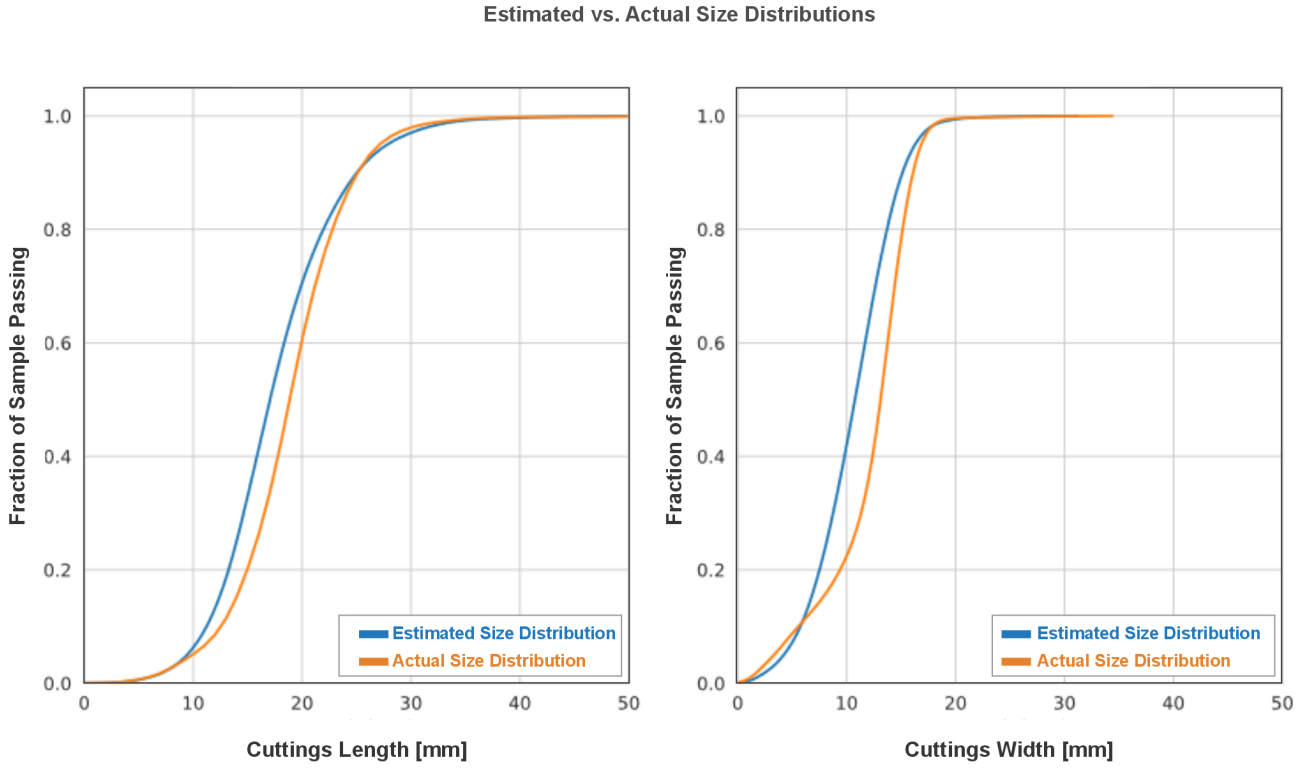



**Fig. 13—Comparison between actual and estimated size distributions of wet, stacked samples.**

cavings result due to tensile failure in near-balance or underbalance conditions while drilling low-permeability formations. Tabular cavings, on the other hand, are related to the invasion of pre-existing weak planes in the rock due to excessive mud density (Skea et al. 2018; Jin et al. 2021; Lopez et al. 2021).

We also performed the morphological classification of cavings using geometrical features and a machine learning model (random forest). These features included (1) length/width ratio, (2) cavings area in the images, (3) the cavings angularity, captured as the area between the caving and the fitted ellipse, and (4) the cavings circularity, captured as the eccentricity of the fitted ellipse. This approach is



Downloaded from http://onepetro.org/SJ/article-pdf/29/10/5238/3677062/spe-217736-pa.pdf/1 by The University of Texas At Austin user on 30 April 2025

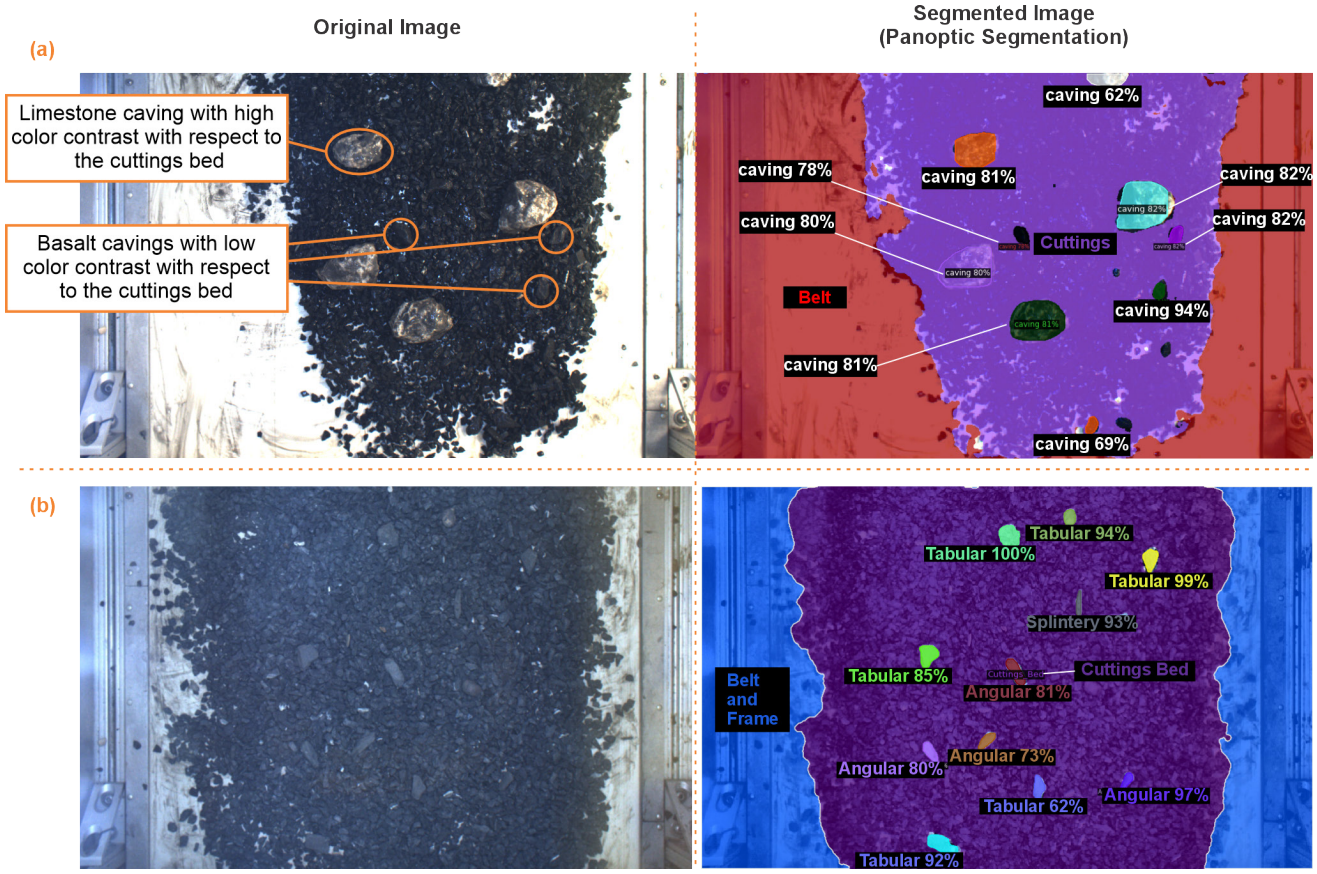



**Fig. 14—Cavings identification with a retrained FPN. This model captures the region corresponding to the belt (and frame), the one corresponding to the cuttings bed, and the individual cavings, including those that have a low color contrast with the cuttings bed. (a) Left: Sample with a dark cuttings bed and cavings of different colors, simulating different color contrast conditions. Right: Segmented mask on top of the original image. (b) Left: Sample with dark cuttings and cavings. Right: Predicted mask with morphological categories of cavings.**

more interpretable because it allows us to better understand why each caving is classified into a specific morphological class. However, we observed that, with this set of features, this approach was less accurate than the panoptic segmentation approach.

## Validation at Laboratory Scale

Rock packings have an inherent void ratio, which is dependent on the rocks' size and shape (White and Walton 1937; Latham et al. 2002; Maroof et al. 2022). As mentioned before, the volume measurement needs to be corrected by taking into consideration this void space. In this section, we will describe the materials and procedures used to compare the estimated volume, which was corrected by the void ratio, and the actual volume of cuttings/cavings. We will show how the proposed methods for segmentation, estimation of the size distribution, and extraction of morphology, are key steps toward accurately correcting the raw volume measured with the laser sensor.

**Materials.** Our experiments involved rock samples of four different classes to simulate cuttings and cavings. These classes were (1) limestone, (2) sandstone, (3) shale, and (4) basalt. These rock samples were sieved and aggregated into groups to control the size distribution in each experiment. This size distribution was later estimated by distributing the sample sparsely on the conveyor belt and implementing the method we introduced in the last section. These samples also varied in color. While basalt and some shale samples were dark in appearance, limestone and sandstone samples were light. The difference in color simulates the common variation in color across cuttings and cavings from different formations. **Table 5** further describes these samples.

| Sample No. | Type of Sample | Nominal Size (mm) | Uniformity | Predominant Shape | Volume (L) |
|---|---|---|---|---|---|
| 1 | Basalt | 4.0 | High | Angular | 2.5 |
| 2 | Basalt | 6.3 | High | Angular | 1.9 |
| 3 | Basalt | 7.9 | Medium | Angular | 1.9 |
| 4 | Basalt | 9.5 | Medium | Angular | 0.7 |
| 5 | Basalt | 12.7 | Medium | Angular | 3.3 |
| 6 | Sandstone + Shale | 4.0 | High | Rounded | 2.0 |

Table 5—Description of the rock samples used in our experiments.



Downloaded from http://onepetro.org/SJ/article-pdf/29/10/5238/3677062/spe-217736-pa.pdf/1 by The University of Texas At Austin user on 30 April 2025

| Sample No. | Type of Sample | Nominal Size (mm) | Uniformity | Predominant Shape | Volume (L) |
|---|---|---|---|---|---|
| 7 | Sandstone + Shale | 6.3 | High | Rounded | 2.0 |
| 8 | Sandstone + Shale | 7.9 | Medium | Rounded | 2.0 |
| 9 | Sandstone + Shale | 9.5 | Medium | Rounded | 2.0 |
| 10 | Sandstone + Shale | 12.7 | Medium | Rounded | 2.5 |
| 11 | Basalt + Shale + Sandstone | 4.0 + 6.3 | Medium | Mixture | 4.2 |
| 12 | Basalt + Shale | 4.0 + 6.3 | Medium | Mixture | 2.4 |
| 13 | Basalt + Limestone + Shale | 4.0 + 6.3+38.1 | Low | Mixture | 4.1 |

Table 5 (continued)—Description of the rock samples used in our experiments.

Some of these rock samples were wetted with mud to test the segmentation techniques under different mud contents. For this purpose, we used a water-based mud prepared with bentonite, barite, and asphalt. The latter was added to force a low contrast between the fluid and the dark rocks, which, in turn, allowed the collection of 2D images that represented a formidable challenge to the segmentation model. This mud had a density of 9.5 ppg, a plastic viscosity of 15 cp, and a yield point of 10 lb/100 $ft^2$.

**Method.** Before the measurement of the samples' actual volume, we allowed a soaking time [as suggested by ASTM C-127 (1993)], to ensure that the rocks were fully saturated. Then, we determined the actual volume of each sample by pouring the sample into a cylindrical container, which was prefilled with water to the top rim. Subsequently, we measured the weight of the water that was displaced by the sample. This weight was then transformed into volume after making the necessary temperature adjustments to the density of the water.

The determination of the void ratio was conducted with a similar setup. However, for this purpose, the sample was loosely shoveled into the cylindrical container, following a procedure similar to the one often utilized for measuring the void ratio of aggregates in civil engineering (BS 812-108 1995). Once these measurements were made, we proceeded to distribute the samples with different arrangements on the conveyor belt. These arrangements ranged from completely sparse to various levels of stacking. Each arrangement was processed with the sensor, which yielded 2D images and 3D PCD associated with each sample.

These data were then fed into our workflow, which yielded (1) the uncorrected volume stemming from the numerical integration of the PCD and (2) the identification and characterization of cuttings and cavings, as described in the previous section. These measurements were repeated to measure the variability in the process. Finally, we compared the actual volume of the samples with the raw/uncorrected volume, determined by executing our workflow. It is important to emphasize that this comparison, which was made in terms of a correction factor, targeted a better understanding of the effect of the size distribution and the morphological description of different samples on the void ratio of the samples in different spatial arrangements. In the following paragraphs, we will describe the results of these measurements.

**Void Space Measurements.** To understand the impact of void space in the required volume correction factor, we first measured the void space of the rock samples. **Fig. 15** showcases some instances of the premoisturized rocks in these samples. As shown in **Fig. 16**, we found a lower void ratio in rounded samples in comparison with angular samples. We also observed a reduced—but existent—dependence of the void ratio on the size distribution. **Fig. 16** also displays the variability of multiple measurements in the form of error bars.

Following the measurement of the actual void spaces, we measured the samples' volumes using the sensor. We observed that the resulting measurement was dependent not only on rock size and morphology but also on the sample stacking level (illustrated in **Fig. 17**). We observed that the higher their stacking, the higher the required volume correction. However, we also noticed that this behavior was not monotonic. Instead, it behaved asymptotically after a certain stacking level. This shows the importance of accounting for the combined



**Fig. 15—Instances of rock samples used in void ratio measurement—basalt angular rocks (left) and sandstone and shale rounded rocks (right).**

Downloaded from http://onepetro.org/SJ/article-pdf/29/10/5238/3677062/spe-217736-pa.pdf/1 by The University of Texas At Austin user on 30 April 2025

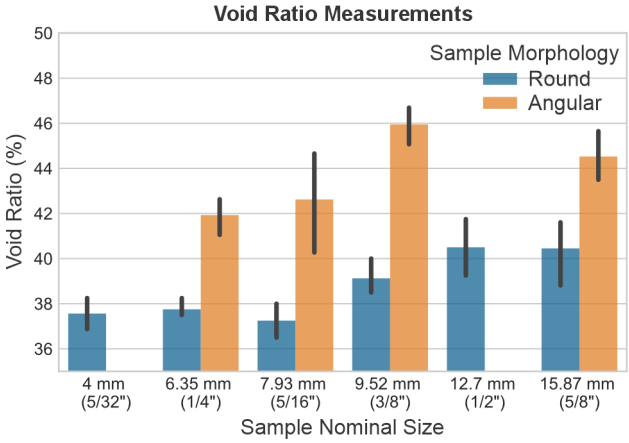



**Fig. 16—Results of void space measurements expressed as the void ratio (ratio of void space to bulk volume: $V_{void\ space}/V_{bulk}$). Each color represents the samples' predominant shape.**

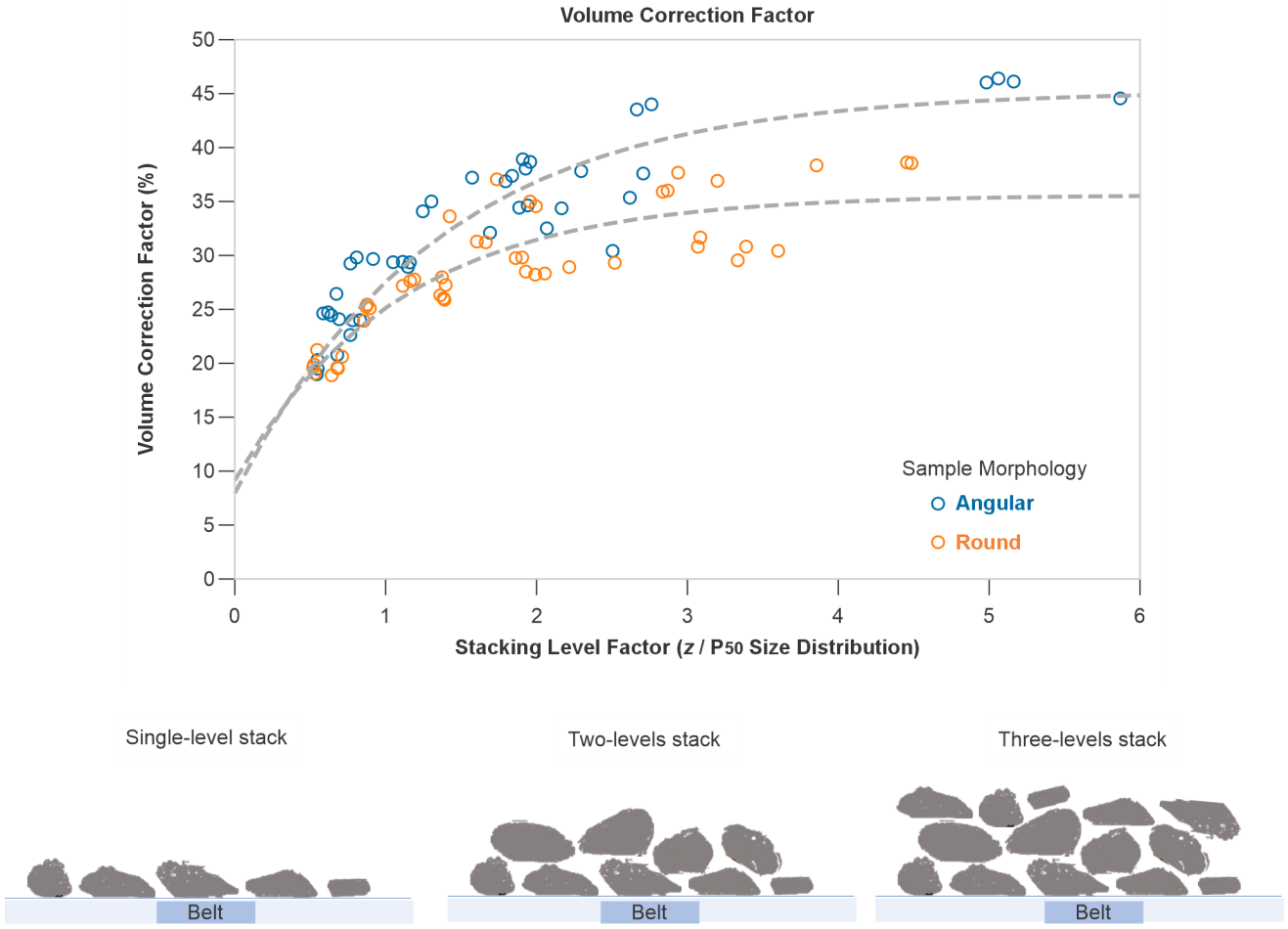



**Fig. 17—(a, top) Volume correction factor as a function of the stacking level factor ($\bar{z}$/P50 size distribution). (b, bottom) Illustration of different stacking levels, captured by stacking level factor.**

effect of rock size/shape and stacking level on the volume correction. For this, we described each arrangement with a stacking level factor as described by Eq. 1:

$$\text{Stacking Level Factor } \left(F_{\text{stacking level}}\right) = \frac{\text{Sample Average Height}}{\text{Sample Median Size}} = \frac{\bar{z}}{\text{Size}_{p_{50}}}. \quad (1)$$



Downloaded from http://onepetro.org/SJ/article-pdf/29/10/5238/3677062/spe-217736-pa.pdf/1 by The University of Texas At Austin user on 30 April 2025

We then computed the volume correction factor, described in Eq. 2, as a function of the stacking level factor described before. **Fig. 17** also describes the volume correction factor as a function of the stacking level factor. As can be observed, the correction factor increases with the staking level factor and reaches an asymptote as the stacking level increases. Furthermore, we observed that, at low stacking levels (associated with a stacking factor less than 2), the volume correction factor does not exhibit a strong dependence on the sample's predominant shape. However, this does not hold for higher stacking factors. As the latter increases, samples with a predominant angular morphology require a higher correction factor than rounded ones:

$$\text{Volume Correction Factor } \left(F_{\text{volume correction}}\right)(\%) = \frac{V_{\text{laser measurement}} - V_{\text{actual volume}}}{V_{\text{laser measurement}}} \times 100. \quad (2)$$

## Discussion

**Volume Measurement.** As mentioned earlier, we corrected the volume measurement to account for the void space, based on the sample stacking level factor described in **Fig. 17**. We then compared these corrected volume measurements with the actual sample volumes, as illustrated in **Fig. 18**.

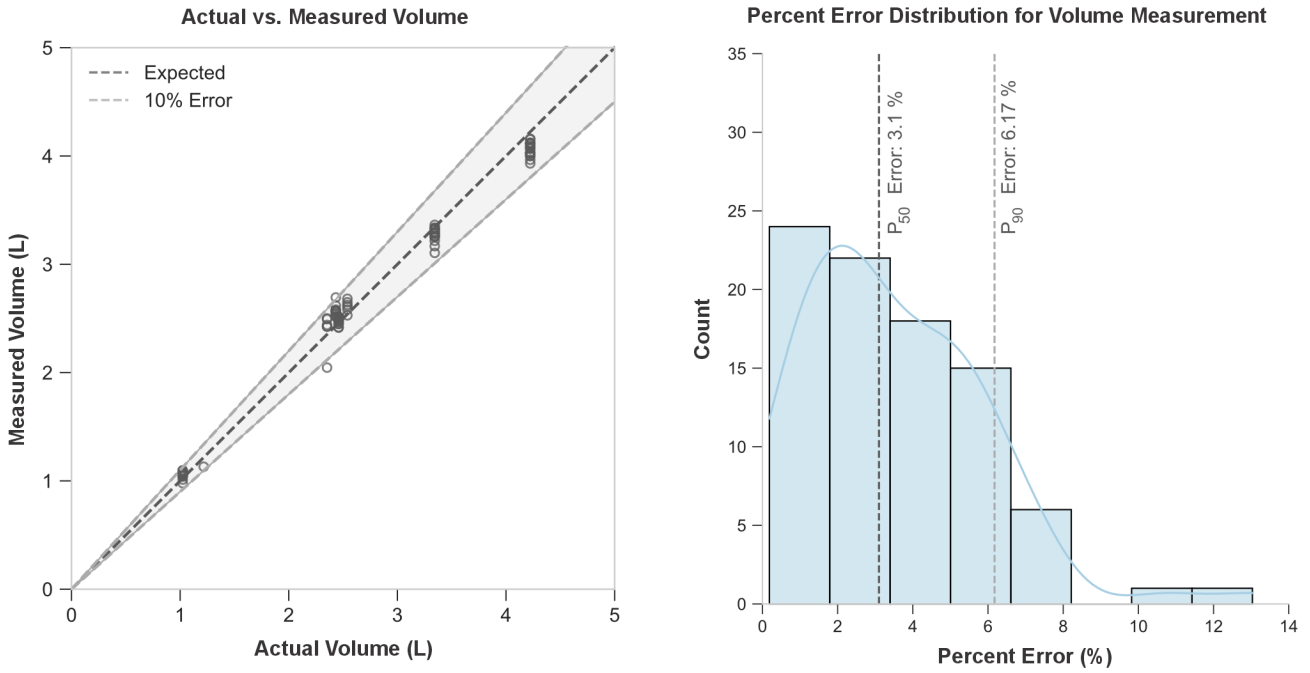



**Fig. 18—(a left) Comparison between actual and corrected volumes of various samples. (b, right) Percent error distribution in volume estimation (right).**

**Fig. 18** illustrates the comparison between actual and measured volumes **(Fig. 18a)**. In the figure, the dashed dark gray diagonal line represents a 0% error, while the light gray lines mark the ±10% error margin. Notably, the corrected volume measurements fall within this 10% error margin. Additionally, **Fig. 18b** presents a distribution of percent errors in volume measurement. The median error (P50) is found to be 3.1%. It is worth mentioning that the majority of measurement errors are below 6.2%, representing the P90 of this distribution. These small errors demonstrate the effectiveness of the volume measurement workflow, which can be applied across a wide range of cuttings shapes and sizes, irrespective of mud content levels and stacking arrangements.

Another important observation is the asymptotic behavior of the correction factor with the level of stacking. This behavior stems from the fact that, at low stacking levels, the void ratio corresponds exclusively to the space below cuttings/cavings, which is registered by the laser scanner as solid. This ratio is not equivalent to the packing void ratio, as it does not reflect the interstitial space between stacked cuttings. Instead, it reflects a "wall effect" with the belt. In the samples that we collected, which represent typical cuttings, this wall effect has a small dependence on the cuttings' size and shape. However, this may not hold for smaller cuttings [this impact of size on the wall effect agrees with Latham et al. (2002)]. For instance, it is possible for the wall effect to become larger in cuttings produced by grinding the rock (such as those produced by impregnated bits). Future development of our work will include the analysis of these types of cuttings.

As stacking increases, the packing void ratio becomes the dominant factor, outweighing the wall effect. Consequently, the volume correction factor exhibits a clear dependence on the shape of cuttings. Rounded cuttings display lower correction factors compared with angular cuttings. This finding aligns with previous studies on void ratio, such as Maroof et al. (2022) and Peronius and Sweeting (1985). In these studies, the authors also describe the importance of accounting for the particles' uniformity (i.e., their sorting). While our method implicitly includes the median size in estimating the stacking factor, it does not account for variations in sample uniformity. Therefore, there is an opportunity to further reduce the already small error in the corrected volume (as shown in **Fig. 18b**) by developing parametric correction factor curves associated with different levels of uniformity.

Finally, it is worth pointing out that the accuracy of the volume estimation depends on the results obtained in the previous steps of our proposed method (refer to **Fig. 2**), including the segmentation and ellipse-fitting steps. A suboptimal segmentation can result in a nonrepresentative morphological description of the cuttings and, consequently, in a nonoptimal correction for void ratio. Our selected models, namely, the mask R-CNN network and ellipse fitting, proved to produce accurate estimations of the cuttings' dimensions. However, such



Downloaded from http://onepetro.org/SJ/article-pdf/29/10/5238/3677062/spe-217736-pa.pdf/1 by The University of Texas At Austin user on 30 April 2025

an accuracy level is affected by the presence of mud. In cases with high mud content, we observed similarity levels (measured with the Bhattacharyya coefficient) of 0.87 and 0.92 between the actual and estimated cuttings' length and width distributions, respectively. Future development of our method will target the reduction of this impact by exploring other segmentation techniques, such as a combined model that uses 2D and 3D data simultaneously.

**Cavings Identification and Classification.** As described earlier, we used two methods for the identification and classification of cavings. The first one relied on the morphological characteristics of each caving, such as their length, width, area, angularity, and circularity. With these features, we trained a random forest classifier. This first approach improved over the one proposed by Han et al. (2018) in two aspects: (1) It incorporated two additional features (angularity, as the area between best-fit ellipses and the segmented cavings, and circularity, as the eccentricity of these ellipses), and (2) it implemented an ensemble of trees, rather than a single decision tree, which reduces the risk of overfitting. The second approach relied on panoptic segmentation employing an FPN. While both approaches reached high levels of detection and classification accuracy (above 80% and 70%, respectively), we will now discuss their differences, as well as their current limitations.

**Table 6** shows the comparison between the detection and classification capabilities of these two approaches. We observed that, for both approaches, the most challenging classification task was associated with angular cavings. Upon deeper examination, we found that most of the misclassified instances were labeled as tabular. Thus, these misclassifications can be related to the fact that tabular cavings contain sharp corners and, thus, well-defined angles. While they typically exhibit a rectangular shape, some tabular cavings can be trapezoidal and resemble triangular cavings. This misclassification reveals the necessity of incorporating additional features, specifically engineered to better distinguish between trapezoidal—or near-triangular—tabular cavings and angular cavings.

| Cavings Morphology | Detection Accuracy | | Classification Accuracy | |
|---|---|---|---|---|
| | Random Forest | Panoptic Segmentation (FPN) | Random Forest | Panoptic Segmentation (FPN) |
| Angular | 0.88 | 1.00 | 0.73 | 0.75 |
| Tabular | 0.87 | 0.96 | 0.76 | 0.96 |
| Splintery | 0.98 | 1.00 | 0.96 | 0.92 |
| Reworked | 0.87 | 0.94 | 0.78 | 0.79 |

Table 6—Cavings identification and classification results.

In terms of cavings detection, we noticed that, despite their accuracy level being above 80%, both approaches missed a few instances of reworked cavings. In these cases, the models erroneously included these cavings in the cuttings bed. Upon deeper examination, we noticed that these instances corresponded to small cavings that approached the median size of the underlying cuttings. These missed instances had a median size of 9.3 mm, while the cuttings bed had a median size of 6.6 mm. It is worth noting that, while we are considering these instances as misclassified, such a small size contrast may exist between cuttings. For instance, a bit that combines crushing and shearing capabilities (such as a PDC-roller cone hybrid bit) may produce heterogeneous cuttings. This reveals the importance of incorporating additional information, such as the type of bit and the formation compressive strength, to reduce the rate of missed small cavings even further.

Another relevant observation is that the panoptic segmentation approach outperforms the random forest approach both in detection and classification capability. This result stems from the fact that the random forest approach relies on a limited, predefined set of features. In contrast, the FPN model extracts the relevant features, automatically, by transforming the original images with a sequence of convolution and subsampling operations. In other words, the model learns these features to maximize its detection and classification performance.

This higher performance comes with a trade-off. The features we defined for the first approach originate from our physical perception of the distinctive characteristics between different types of cavings, which increases the model interpretability. In the second approach, on the other hand, the features are encapsulated in a complex sequence of transformations within the model internal logic. This results in a noninterpretable model. Despite this disadvantage, the second approach can be coupled, in the future, with explainable machine learning techniques. These techniques seek to explain how the classification outputs of noninterpretable models are associated with specific parts of the images. Although these techniques are currently considered undeveloped by many authors and therefore not suitable for high-stakes decision scenarios, future development of this field can potentially lead to trustworthy models, applicable to our case (Linardatos et al. 2020).

Finally, it is worth noting that the comparison and performances presented in **Table 6** hold for the morphological features used in the first approach, the image preprocessing methods, and the training/testing samples used in the second approach. Our empirical evidence suggests that employing panoptic segmentation leads to higher detection and classification rates of cavings. However, it is possible that, with the inclusion of more informative features, the first approach may achieve a higher level of accuracy compared with the second one. Our future work will include the enhancement of the first approach in this regard, as well as the use of actual cuttings and cavings from drilling operations.

## Conclusions

We have developed a novel and accurate method for real-time characterization of cuttings and cavings, including volume, size distribution, and shape/morphology. This method combines 2D images with 3D data collected through a fully integrated sensor, enabling precise characterization of cuttings/cavings even under challenging field conditions. Our results lead us to conclude the following:

- Identifying individual cuttings and cavings (segmentation) is fundamental for their accurate characterization and, ultimately, volume estimation.
- Optimized image preprocessing techniques are crucial for precise segmentation. These include (1) image denoising, (2) histogram equalization, (3) image thresholding, and (4) morphological optimization.
- Deep CNNs are highly effective in the identification and classification of individual cuttings/cavings (segmentation) in real time. Specifically, a modified VGG-16 CNN has shown high accuracy in identifying the presence of mud; a mask R-CNN model proved

Downloaded from http://onepetro.org/SJ/article-pdf/29/10/5238/3677062/spe-217736-pa.pdf/1 by The University of Texas At Austin user on 30 April 2025

suitable for identifying individual cuttings (instance segmentation); and an FPN showed robustness in identifying individual cavings and extracting the area-based cavings-to-cuttings ratio (panoptic segmentation).

- In distinguishing between different classes of cavings (e.g., angular, splintery, tabular, and reworked), the FPN model appears to outperform a random forest classifier based on morphological characteristics (e.g., width/length ratio, cavings area, circularity, and angularity). This observation, however, is specific to our sample set. The use of other morphological features, to be investigated in future work, may enhance the random forest classifier.
- Both the FPN and the random forest classification methods demonstrate accuracy levels that facilitate precise and real-time diagnosis of drilling anomalies/dysfunctions, such as insufficient mud density or excessive drilling fluid filtration into pre-existing weak planes in the formation (e.g., fractures or bedding planes).
- Our method is versatile and not limited to optimal shale shaker conditions (e.g., sparse and dry cuttings). It remains accurate in challenging scenarios, such as when cuttings/cavings are wet, have low color contrast with the mud, or are stacked due to suboptimal operational conditions.
- The initial estimate of cuttings volume, based on the numerical integration of the 3D reconstructed profile, requires an adjustment to account for the void space among cuttings and between cuttings and the belt. This volume adjustment depends on the stacking level (height of the cuttings stack), size distribution, and shape of the cuttings/cavings. The required adjustment increases with stacking level up to a certain point, beyond which it behaves asymptotically.
- At high stacking levels, rounded cuttings/cavings require a smaller volume correction than angular ones, consistent with prior research on the void ratio of particle aggregates. At lower stacking levels (stacking factor less than 2), the volume correction is not influenced by morphology but rather by the empty space between the cuttings and the belt—termed the "wall effect."

Future development of our proposed method includes its integration with a transient cuttings-transport model, as well as with a robust geomechanical model, to provide real-time assessment of the wellbore condition in terms of hole cleaning sufficiency and wellbore stability. In addition, this real-time assessment will be coupled with drilling incident detectors/predictors—such as stuck pipe prediction models—to study the potential increase of their detection capability and enhance the fidelity of the produced incident warnings.

In addition, while our proposed method relies on the separate processing of 2D and 3D data, producing reliable results even in nonoptimal conditions, we will investigate an alternative, integrated, and potentially more accurate approach in the future. This alternative approach will involve identifying individual solids by simultaneously leveraging both types of data (2D and 3D) in a unique segmentation algorithm. Finally, although the samples used in our study are representative, we will extend our analysis of the volume correction factor by compiling larger samples corresponding to actual cuttings and cavings in the field.

## Acknowledgments

The authors thank the members of the Rig Automation and Performance Improvement in Drilling (RAPID) industry affiliate program at The University of Texas at Austin for the financial support provided for this study.

## References

Andersson, T., Thurley, M. J., and Carlson, J. E. 2012. A Machine Vision System for Estimation of Size Distributions by Weight of Limestone Particles. *Miner Eng* **25** (1): 38–46. https://doi.org/10.1016/j.mineng.2011.10.001.

ASTM C-127, *Standard Test Method for Relative Density (Specific Gravity) and Absorption of Coarse Aggregate*. 1993. West Conshohocken, Pennsylvania, USA: ASTM International. https://doi.org/10.1520/C0127-15.2.

Badis, C., Souza, W., Yasir, M. A. et al. 2021. Machine Learning/Artificial Intelligence Driven Computer Vision for Cuttings Analysis Under Drilling and Completions. Paper presented at the SPE Eastern Europe Subsurface Conference, Kyiv, Ukraine, 23–24 November. https://doi.org/10.2118/208509-MS.

BS 812-108, *Methods for Determination of Bulk Density, Optimum Moisture Content, Voids and Bulking*. 1995. London, UK: British Standards Institution.

Campello, R. J. G. B., Moulavi, D., and Sander, J. 2013. Density-Based Clustering Based on Hierarchical Density Estimates. In *Adv Knowl Discov Data Min (2017)*, eds. J. Pei, V. S. Tseng, L. Cao, et al., 160–172. Berlin, Heidelberg: Lecture Notes in Computer Science, Springer. https://doi.org/10.1007/978-3-642-37456-2_14.

Chen, Q., Yang, X., and Petriu, E. M. 2004. Watershed Segmentation for Binary Images with Different Distance Transforms. Paper presented at the 3rd IEEE International Workshop on Haptic, Audio and Visual Environments and Their Applications - HAVE 2004, Ottawa, Ontario, Canada, 2–3 October. https://doi.org/10.1109/HAVE.2004.1391891.

Di, K., Yue, Z., Liu, Z. et al. 2013. Automated Rock Detection and Shape Analysis from Mars Rover Imagery and 3D Point Cloud Data. *J Earth Sci* **24** (1): 125–135. https://doi.org/10.1007/s12583-013-0316-3.

Du, X., Jin, Y., Wu, X. et al. 2020. Classifying Cutting Volume at Shale Shakers in Real-Time Via Video Streaming Using Deep-Learning Techniques. *SPE Drill & Compl* **35** (03): 317–328. https://doi.org/10.2118/194084-PA.

Girdner, K. K., Kemeny, J. M., Srikant, A. et al. 1996. The Split System for Analyzing the Size Distribution of Fragmented Rock. In *Measurement of Blast Fragmentation*, eds. J. A. Franklin and T. Katsabanis. Rotterdam, The Netherlands: A. A. Balkema.

Girshick, R. 2015. Fast R-CNN. Paper presented at the 2015 IEEE International Conference on Computer Vision (ICCV), Santiago, Chile, 7–13 December. https://doi.org/10.1109/ICCV.2015.169.

Graves, A. and Rowe, M. 2014. Down Hole Cuttings Analysis. US Patent no.2014/0333754 A1.

Grossi, C. D., Hummels, Y. H., Meleiros, L. A. da C. et al. 2023. Cuttings Return Analysis by Visual Imaging: Novel Technology to Support Drilling Automation. Paper presented at the SPE/IADC International Drilling Conference and Exhibition, Stavanger, Norway, 7–9 March. https://doi.org/10.2118/212441-MS.

Guo, Q., Wang, Y., Yang, S. et al. 2022. A Method of Blasted Rock Image Segmentation Based on Improved Watershed Algorithm. *Sci Rep* **12** (1). https://doi.org/10.1038/s41598-022-11351-0.

Gupta, A., Dollar, P., and Girshick, R. 2019. LVIS: A Dataset for Large Vocabulary Instance Segmentation. Paper presented at the 2019 IEEE/CVF Conference on Computer Vision and Pattern Recognition (CVPR), Long Beach, California, USA, 15–20 June. https://doi.org/10.1109/CVPR.2019.00550.

Han, R., Ashok, P., Pryor, M. et al. 2017. Real-Time Borehole Condition Monitoring Using Novel 3D Cuttings Sensing Technology. Paper presented at the SPE/IADC Drilling Conference and Exhibition, The Hague, The Netherlands, 14–16 March. https://doi.org/10.2118/184718-MS.

Han, R., Ashok, P., Pryor, M. et al. 2018. Real-Time 3D Computer Vision Shape Analysis of Cuttings and Cavings. Paper presented at the SPE Annual Technical Conference and Exhibition, Dallas, Texas, USA, 24–26 September. https://doi.org/10.2118/191634-MS.

Downloaded from http://onepetro.org/SJ/article-pdf/29/10/5238/3677062/spe-217736-pa.pdf/1 by The University of Texas At Austin user on 30 April 2025

He, K., Gkioxari, G., Dollar, P. et al. 2020. Mask R-CNN. *IEEE Trans Pattern Anal Mach Intell* **42** (2): 386–397. https://doi.org/10.1109/TPAMI.2018.2844175.

Holt, C. and Ruel, F. 2022. Using AI Cuttings Load Classification to Assess Hole Cleaning and Wellbore Stability. Paper presented at the SPE Annual Technical Conference and Exhibition, Houston, Texas, USA, 3–5 October. https://doi.org/10.2118/210369-MS.

Jin, J., Jin, Y., Lu, Y. et al. 2021. Classification and Mechanism Analysis of Wellbore Failure Based on Cavings. Paper presented at the 55th U.S. Rock Mechanics/Geomechanics Symposium, Virtual, 18–25 June. ARMA-2021-1623.

Jin, J., Jin, Y., Lu, Y. et al. 2022. Image Processing and Machine Learning Based Cavings Characterization and Classification. *J Pet Sci Eng* **208**: 109525. https://doi.org/10.1016/j.petrol.2021.109525.

Jing, H., Ozbayoglu, E., Baldino, S. et al. 2024. AI Camera System for Real-Time Load Concentration Estimation. Paper presented at the Offshore Technology Conference, Houston, Texas, USA, 18–25 June. https://doi.org/10.4043/35171-MS.

Kirillov, A., He, K., Girshick, R. et al. 2019. Panoptic Segmentation. Paper presented at the 2019 IEEE/CVF Conference on Computer Vision and Pattern Recognition (CVPR), Long Beach, California, USA, 15–20 June. https://doi.org/10.1109/CVPR.2019.00963.

Kirillov, A., Mintun, E., Ravi, N. et al. 2023. Segment Anything. arXiv:2304.02643 (preprint; submitted 5 April 2023). https://doi.org/10.48550/arXiv.2304.02643.

Latham, J.-P., Munjiza, A., and Lu, Y. 2002. On the Prediction of Void Porosity and Packing of Rock Particulates. *Powder Technology* **125** (1): 10–27. https://doi.org/10.1016/S0032-5910(01)00493-4.

Linardatos, P., Papastefanopoulos, V., and Kotsiantis, S. 2020. Explainable AI: A Review of Machine Learning Interpretability Methods. *Entropy (Basel)* **23** (1): 1–18. https://doi.org/10.3390/e23010018.

Lin, T.-Y., Dollar, P., Girshick, R. et al. 2017. Feature Pyramid Networks for Object Detection. Paper presented at the 2017 IEEE Conference on Computer Vision and Pattern Recognition (CVPR), Honolulu, Hawaii, USA, 21–26 July. https://doi.org/10.1109/CVPR.2017.106.

Lopez, C. F., Mateus, J. S., Arias, H. et al. 2021. Practical Approach for Wellbore Stability Modelling in a Tectonically and Geologically Complex Area: Colombian Foothills Field Case. Paper presented at the ISRM 9th International Symposium on Geomechanics, Virtual, 5–6 May. ISRM-ISG-2021-10.

Marana, A. N., Guilherme, I. R., Papa, J. P. et al. 2010. An Intelligent System to Detect Drilling Problems Through Drilled Cuttings Return Analysis. Paper presented at the IADC/SPE Drilling Conference and Exhibition, New Orleans, Louisiana, USA, 2–4 February. https://doi.org/10.2118/128916-MS.

Maroof, M. A., Mahboubi, A., Vincens, E. et al. 2022. Effects of Particle Morphology on the Minimum and Maximum Void Ratios of Granular Materials. *Granular Matter* **24** (1): 1–41. https://doi.org/10.1007/s10035-021-01189-0.

Moore, P. 1986. *Drilling Practices Manual*, second edition. Tulsa, Oklahoma, USA: PennWell Publishing.

Mulchrone, K. F. and Choudhury, K. R. 2004. Fitting an Ellipse to an Arbitrary Shape: Implications for Strain Analysis. *J Struct Geol* **26** (1): 143–153. https://doi.org/10.1016/S0191-8141(03)00093-2.

Murchinson, W. 1982. *Murchinson Drilling Manual*, first edition. Albuquerque, New Mexico, USA: Murchinson Drilling Schools.

Naegel, M., Pradie, E., Delahaye, T. et al. 1998. Cuttings Flow Meters Monitor Hole Cleaning in Extended Reach Wells. Paper presented at the European Petroleum Conference, The Hague, Netherlands, 20–22 October. https://doi.org/10.2118/50677-MS.

Nanjo, T., Ebitani, A., Ishikawa, K. et al. 2023. Automatic Lithology Classification of Cuttings with Deep Learning. Paper presented at the International Petroleum Technology Conference, Bangkok, Thailand, 1–3 March. https://doi.org/10.2523/IPTC-22867-EA.

Peronius, N. and Sweeting, T. J. 1985. On the Correlation of Minimum Porosity with Particle Size Distribution. *Powder Tech* **42** (2): 113–121. https://doi.org/10.1016/0032-5910(85)80043-7.

Prez, S., Callerio, S., Montes, A. et al. 2023. Field Testing of an Automated 3D Cuttings and Cavings Measurement Sensor. Paper presented at the SPE/IADC International Drilling Conference and Exhibition, Stavanger, Norway, 7–9 March. https://doi.org/10.2118/212569-MS.

Ronneberger, O., Fischer, P., and Brox, T. 2015. U-Net: Convolutional Networks for Biomedical Image Segmentation. In *Medical Image Computing and Computer-Assisted Intervention – MICCAI 2015*, eds. N. Navab, J. Hornegger, and W. Wells. et al, 234–241. Cham, Switzerland: Lecture Notes in Computer Science, Springer. https://doi.org/10.1007/978-3-319-24574-4_28.

Saasen, A., Omland, T. H., Ekrene, S. et al. 2009. Automatic Measurement of Drilling Fluid and Drill-Cuttings Properties. *SPE Drill & Compl* **24** (04): 611–625. https://doi.org/10.2118/112687-PA.

Simonyan, K. and Zisserman, A. 2015. Very Deep Convolutional Networks for Large-Scale Image Recognition. arXiv:1409.1556 (preprint; last revised 10 April 2015). https://doi.org/10.48550/arXiv.1409.1556.

Skea, C., Rezagholilou, A., Behnoud Far, P. et al. 2018. An Approach for Wellbore Failure Analysis Using Rock Cavings and Image Processing. *J Rock Mech Geotech Eng* **10** (5): 865–878. https://doi.org/10.1016/j.jrmge.2018.04.011.

Szegedy, C., Vanhoucke, V., Ioffe, S. et al. 2016. Rethinking the Inception Architecture for Computer Vision. Paper presented at the 2016 IEEE Conference on Computer Vision and Pattern Recognition (CVPR), Las Vegas, Nevada, USA, 27–30 June. https://doi.org/10.1109/CVPR.2016.308.

Thonhauser, G., Maidla, E., O'Leary, P. et al. 1999. Rigsite Measurement of Cuttings Weight Equipment: Method to Analyze the Data and Extended-Reach Field Test. Paper presented at the SPE Annual Technical Conference and Exhibition, Houston, Texas, USA, 3–6 October. https://doi.org/10.2118/56561-MS.

Thurley, M. J. 2013. Automated Image Segmentation and Analysis of Rock Piles in an Open-Pit Mine. Paper presented at the International Conference on Digital Image Computing: Techniques and Applications, Hobart, Tasmania, Australia, 26–28 November. https://doi.org/10.1109/DICTA.2013.6691484.

Torrione, P. 2021. System and Method for Estimating Cuttings Volumes on Shale Shakers. US Patent No.10,954,729 B2.

Wang, W. 2006. Image Analysis of Particles by Modified Ferret Method — Best-Fit Rectangle. *Powder Tech* **165** (1): 1–10. https://doi.org/10.1016/j.powtec.2006.03.017.

Wang, J., Wang, Y., Wang, J. et al. 2023. Design of an Image Segmentation System Based on Hierarchical Density-Based Spatial Clustering of Applications with Noise for Off-Road Unmanned Ground Vehicles. In *Proceedings of 2022 International Conference on Autonomous Unmanned Systems (ICAUS 2022)*, eds. W. Fu, M. Gu, and Y. Niu, 3163–3175. Singapore: Lecture Notes in Electrical Engineering, Springer. https://doi.org/10.1007/978-981-99-0479-2_291.

White, H. E. and Walton, S. F. 1937. Particle Packing and Particle Shape. *Journal of the American Ceramic Society* **20** (1–12): 155–166. https://doi.org/10.1111/j.1151-2916.1937.tb19882.x.

Wu, Y., Kirillov, A., Massa, F. et al. 2021 Detectron 2. https://github.com/facebookresearch/detectron2.

Downloaded from http://onepetro.org/SJ/article-pdf/29/10/5238/3677062/spe-217736-pa.pdf/1 by The University of Texas At Austin user on 30 April 2025